Optimization of a Non-axial Magnet Design for a Hybrid Radiation Treatment and MR Imaging System

by

Shima Yaghoobpour Tari

A thesis submitted in partial fulfillment of the requirements for the degree of

Master of Science
in
Medical Physics

Department of Oncology
University of Alberta

Abstract

A prototype rotating hybrid magnetic resonance (MR) imaging system and linac has been developed to allow for simultaneous imaging and radiation delivery parallel to B_o. However, the design of a compact magnet capable of rotation in a small vault with sufficient patient access and a typical clinical source-to-axis distance (SAD) is challenging. This work presents a novel superconducting magnet design that allows for a reduced SAD and ample patient access by moving the superconducting coils to the side of the yoke. The yoke and pole-plate structures are shaped to direct the magnetic flux appropriately.

A closed symmetrical system with different pole plate structures was studied to find the most suitable optimization algorithm and pole plate structure. Then, the outer surface of the pole plate for a non-axial design was optimized subject to the minimization of a cost function, which evaluates the uniformity of the magnetic field over an ellipsoid. This non-axial design is reminiscent of a C-core transformer. Magnetic field calculations were performed with the 3D finite element method (FEM) software package Opera-3D. Each tentative design strategy was virtually modeled in this software package, which is externally controlled by MATLAB, with its key geometries defined as variables. The optimization variables were the thickness of the pole plate at control points distributed over the pole plate surface.

Optimized magnet assemblies that generate homogenous 0.2T and 0.5T magnetic fields over an ellipsoid with a large axis of 60 cm and small axes of 40 cm were obtained.

The distinct features of this model are the minimal distance between the yoke's top and the isocentre, which allows for a minimal SAD, and the improved patient access. Additionally, obtaining field homogeneity over a large field-of-view leads to a unit with enhanced imaging flexibility.

Acknowledgements

First and foremost I would like to express my appreciation for Dr. Keith Wachowicz, for all his contributions of ideas and time throughout this work. His patience and encouragement were the motivating forces to keep me going during all ups and downs. It was a pleasant experience to work with Keith as I always felt welcome to ask for his guidance whenever I needed it.

I would like to express my sincere gratitude to Dr. B. Gino Fallone for giving me the chance to be part of the Linac-MR team, for his valuable feedback during the work, and for the financial support. His ambition and persistence to pursue his goal will always inspire me.

I would like to thank my supervisory and defense committee Dr. Nicola DeZanche, Dr. Matt Larocque, Dr. Joel St. Aubin, and Dr. Brad Warkentin. My special thanks for Drs. Nicola DeZanche and Joel St. Aubin for their useful feedback during the supervisory committee meetings.

I would like to gratefully acknowledge the support that I received from the medical physics group at the Cross Cancer Institute. Many thanks to Heather Warkentin for taking your time to listen to me, and provide information and guidance whenever I needed it. Thanks Brie for being a great friend and thanks Ray for being such an encouraging officemate.

I would like to extend my acknowledgement to Marjie, Phil, Mina, Shiva, Shadi, AmirMohammad, and my parents for their unconditional love and support.

Table of Contents

List of Tables

List of Figures

Chapter 1

Introduction

External beam radiation is a common type of radiotherapy for cancer treatment where the radiation source is located outside the patient's body. For this treatment, high-energy radiation consisting of photons or charged particles (electron, proton, or heavy ions) are delivered to the tumor. The medical linear accelerator (linac) is the source most commonly used to generate either the high-energy electron beam used to treat the superficial tumors, or the high-energy photons used to treat the deep-seated tumors.

The clinical goal of radiotherapy is to deliver the highest dose to the tumor, thereby maximizing the tumor control probability (TCP), while sparing as much normal tissue as possible and minimizing the normal tissue complication probability (NTCP). To achieve this goal, the treatment that is delivered should match the treatment that was planned. However, there are always uncertainties associated with both the planning and delivery of radiotherapy.

Treatment uncertainties can be related to patient set-up, variation in tumor size over the course of treatment, or motion of the tumor during the treatment. To account for the uncertainties, volumes and margins are defined with respect to target anatomy for the treatment planning[1;2], shown in figure (1.1). The gross tumor volume (GTV) is the gross visible extent of cancerous tissue. The clinical target volume (CTV) includes the GTV and microscopic spread of the malignant tissue, which requires sufficient dose to be eliminated. An internal margin (IM) is added to the CTV to account for any target motion and size and shape variation of the CTV during the treatment. The CTV with the added margin is called internal target volume (ITV)[2]. A set-up margin (SM) is added to the ITV to account for patient set-up; this final volume is called the planning target volume (PTV).

Based on the aforementioned tumor and target volume definitions, any healthy tissue within the PTV is undesirably irradiated, leading to possible adverse tissue complications. Intensity-modulated radiotherapy (IMRT) tackles this issue by delivering a conformal dose distribution to the PTV using a sharp dose gradient. However, it is important to avoid any positioning errors related to the PTV while using highly conformal techniques such as IMRT. Hence, imaging systems have been developed to provide information about the position of the tumor and its motion for Image-Guided RadioTherapy (IGRT). The quality of radiotherapy has improved drastically by combining conformal radiotherapy with IGRT.

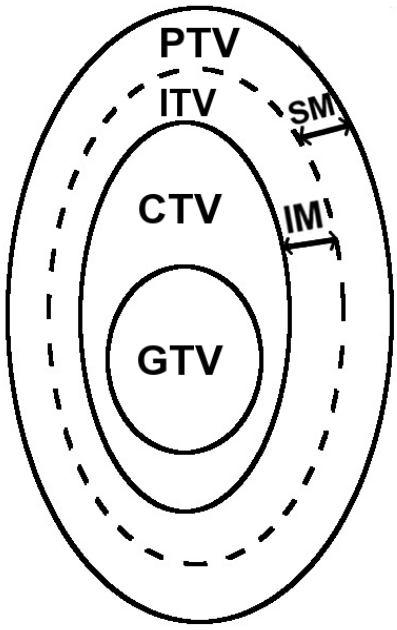

Figure 1.1: Volumes and margins defined by the International Commission on Radiation Units (ICRU): gross tumor volume (GTV), clinical target volume (CTV), internal margin (IM), internal target volume (ITV), set-up margin (SM), and planning target volume (PTV).

1.1 Image-Guided Radiotherapy

IGRT is defined as the use of frequent imaging in the treatment room allowing for adjustments that reduce geometrical errors in patient set-up and account for geometrical changes of the tumor. The goal of IGRT is to reduce the CTV to PTV margins, thereby reducing healthy tissue irradiation[3;4]. A wide variety of imaging modalities, including planar megavoltage (MV) and kilovoltage (kV) imaging, cone beam computed tomography (CBCT), and 3D ultrasound, are used to increase the accuracy of the treatment by the use of the IGRT.

On-board IGRT devices are MV and kV imagers attached to the linac. An electronic portal imaging device (EPID) is a portal megavoltage (MV) imager, which uses the treatment beam and flat-panel imaging detector to obtain a two-dimensional image. An EPID can also be used for dose measurements, and it is considered as a useful tool for quality assurance and plan verification of IMRT treatment plans[5;6]. MV images suffer from poor soft tissue contrast and the superposition of other structures onto a 2D image decreases the contrast further. In addition, an additional dose is received by the patient during the MV imaging. Another on-board imager is the kilovoltage (kV) imager, where the X-ray source and detector system are perpendicular to the treatment beam axis. The contrast can be improved and a lower dose is delivered to the patient when the kV beam is used. Real-time tracking markers implanted in lung tumors, using fluoroscopic kV imaging, have been proposed[7].

Volumetric 3D images can be obtained using the on-board imagers. Cone-beam computed tomography (CBCT) images are acquired from projection images taken at different angles as the gantry is rotated through the beam axis. However, it is not possible to do volumetric imaging while the treatment beam is on. Also, CBCT has limitations for localizing tumors within the soft tissue due to the poor soft tissue contrast compared to medical CT scanner or MRI. Therefore, the use of the CBCT images is limited to positioning the patient before the treatment.

Tomotherapy is a type of radiotherapy that combines the geometry of a CT imager with the beam of a linac. The rotating MV beam delivers highly con-

formal IMRT, slice-by-slice, as the patient is translated longitudinally through the bore[8]. The MVCT images can be used for patient setup, tumor alignment, and treatment verification[9]. Similar to other imaging devices with X-ray sources, extra dose is delivered to the patient. The dose from a single scan might be quite low compared to the prescribed dose, but the accumulative dose due to the day-to-day treatment should be considered. Furthermore, the helical MVCT can not be used for the real-time motion tracking since the imaging and treatment sources are the same.

Other modalities used for IGRT include ultrasound (US), or electromagnetic field tracking, where no ionization radiation is involved. However, these modalities have limitations. US can be used to visualize soft tissues and assist with target localization prior to the treatment planning[10;11]. The limitation of US is the required presence of an operator, which makes it unusable for real-time tracking. In addition, the anatomic diplacement caused by the pressure of the imaging probe is a concern[12]. In electromagnetic field tracking, an electromagnetic transponder is implanted near the tumor and is electromagnetically tracked in real-time from outside the patient[13]. The limitation for this technique is the lack of volumetric information obtained about the tumor. It also requires an additional invasive procedure for the patient, and there is the possibility that the implants may migrate after implantation.

As mentioned, current imaging modalities for IGRT have limitations in one or more aspects, which make them unsuitable to provide real-time imaging during treatment. However, magnetic resonance (MR) imaging has been found

to be a good choice for this task. MR can produce images with exquisite soft tissue contrast helping to improve accuracy of the delineation of both tumor and surrounding tissues. In addition, no ionizing radiation is involved during the imaging process, so no extra dose is received by the patient. Given these imaging abilities, a hybrid system combining a radiation treatment unit and an MR imager would permit real-time image-guided radiotherapy, where a continuous stream of images throughout the radiation treatment could be acquired. As a result, any tumor motion could be identified, and the radiation beam could be adapted to accommodate the change. Having the beam precisely on the target during the treatment would minimize the harm to normal tissue near the tumor. The following section describes the developments in the use of MR imaging for real-time IGRT.

1.2 Real-Time MRI-Guided Radiotherapy

There has been an increasing interest in using MR imaging in radiotherapy in the recent years. At the present time, there are a number of prototypes for hybrid radiation treatment and MR imaging systems both in production and development [14;15;16;17;18].

One commercially available system is the ViewRay system designed for MR-guided IMRT [14;19;20]. This system consists of a double-doughnut 0.35 T superconducting magnet, with a vertical gap to mount three ^{60}Co sources on a ring gantry. The advantage of this system is the lack of radio frequency (RF) interference between the ^{60}Co beams and MR imager. However, the charac-

teristics of the ^{60}Co beam, such as larger penumbra, less penetrating power, higher surface dose, and lower output compared to a linac, are disadvantages of this system[14].

A group at the UMC Utrecht, Netherlands, has constructed a prototype consisting of a modified 1.5 T Philips Achieva MR system integrated with a modified 6 MV Elekta accelerator[16;21]. The redesigned stationary magnet has a central region that is free of coils, opening a path for the beam. In addition, a low-field toroidal zone is formed using active shimming to locate the electron gun of the linac. The use of a 1.5 T field increases the signal to noise ratio, which is an advantage of this system. However, the radiation beam is perpendicular to the magnetic field for this system, which creates hot and cold spots in the dose distribution at tissue-air interfaces, particularly apparent at this higher field strength[22;23]. This is due to the electron return effect, where the Lorentz force on moving electrons results in the return of the electrons back to the tissue at the beam exit point. This could be considered a drawback of this system, and needs to be accounted for during treatment planning, especially for lung, head, and neck cancers[21].

Our research group at the Cross Cancer Institute (CCI) in Edmonton, Alberta, Canada has built prototypes of integrated linac-MR systems[17;18;24] in two phases. The development of these prototypes will be explained in the following section.

1.2.1 Linac-MR System

The Linac-MR system is designed as a 6 MV linac mounted onto a bi-planar rotating MR scanner to allow for simultaneous imaging and radiation delivery. The rotating bi-planer magnet permits two different potential orientations of the radiation source with respect to the magnetic field: the perpendicular and parallel configurations. Hence, one of the unique features of this rotating design is the ability to transmit radiation parallel to the the B_o field, which has been shown to have dosimetric advantages compared to the perpendicular configuration[18]. These advantages take the form of a reduced penumbra width[25], reduction of tissue-air interface effects, and increased dose in the PTV, resulting in an overall reduction in dose to the surrounding normal tissue[26].

For phase I, an integrated system of a 6 MV linac with an optimized permanent magnet sized for head imaging was built. The installation and mechanical rotation of the magnet for this system was easier because of the absence of cryostat for cooling and relative lack of electrical wiring. A low magnetic field (0.2 T) can be achieved using permanent magnets, which lead to weak fringe fields and simplification of the linac magnetic shielding. The limitation of this system is the challenge of obtaining the desired homogeneity over a large field view, while still satisfying the dimensional constraints for the Linac-MR system[27;28]. The lateral dimension and pole diameter are constrained as the system should be able to rotate within a typical radiotherapy vault. The permanent-magnet system was built to check the viability of the

integration of two systems, and the world's first MR image acquired during irradiation was obtained by this system[17;24].

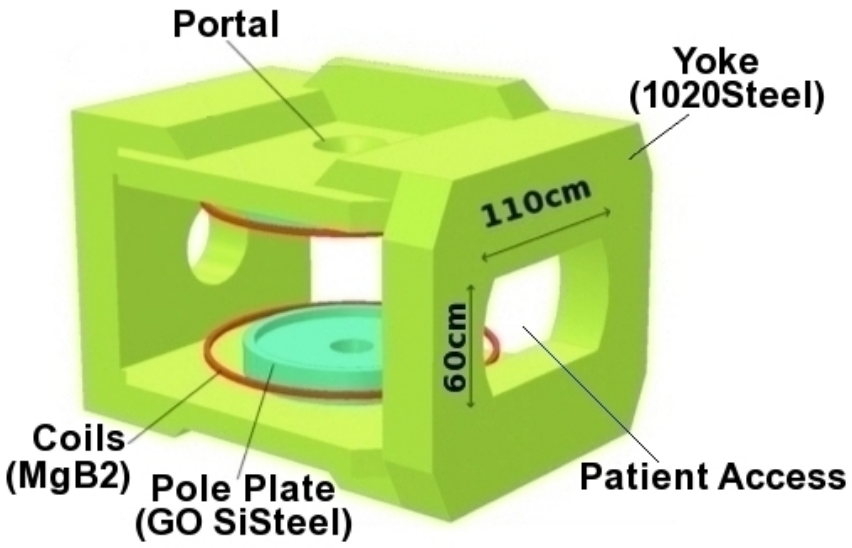

Figure 1.2: 3-D schematic of the bi-planar magnet with dimensions representative of the Linac-MR $v2$ system.

A hybrid system of a 6 MV linac and an optimized cryogen-free high-temperature superconducting (HTS) magnet was developed and built for the second phase[17]. The superconducting magnet can produce higher fields, which improves the image quality and acquisition speeds. There are two versions of the superconducting magnet as a commercial whole-body open-bore magnet. Our $v1$ system with a 0.5 T field has a source-to-axis distance (SAD) of 126 cm[18] and the gap between two pole plates is 60 cm[17]. The $v2$ system, generating a 0.5 T magnetic field, has a SAD of 130 cm[18], and a rectangular opening with width of 110 cm and height of 60 cm for patient access. Three-

dimensional illustration of the bi-blanar magnet for the $v2$ system is shown in (1.2). The SAD is increased for the $v2$ system, which reduces the dose rate[18].

The linac system rotates around the isocentre, which is the intersection of the rotation axis of the gantry and the central axis of the radiation beam. To avoid patient repositioning for every beam angle during the treatment, an isocentric method is used to deliver the radiation, where the target volume centre is placed at the isocentre throughout the radiation. However, it is difficult, if not impossible, to apply the same technique for the patient with a peripheral tumor while using one of the hybrid of MR and radiotherapy systems mentioned in the previous section. Considering the cylindrical nature of the magnet with a bore of about 60 cm, it is difficult to position a patient with his or her peripheral tumor positioned at isocentre.

For the Linac-MR system, the bi-planar nature of the magnet allows for a wide-range of motion in a direction parallel to the face of the pole plate and perpendicular to the radiation beam. Given that, a peripheral tumor treatment positioning (PTTP) system and method, explained in detail in[29], can be employed to make sure that the tumor is always kept in the axis of the beam. Based on this method, a central position and a treatment position are defined for the couch positioning. The collision between the patient and the rotating Linac-MR system is prevented as long as the couch is located at the central position. The treatment position is calculated based on the gantry angle. At any specific angle, the couch is moved to the treatment position for delivering the treatment then it is reversed to the central position for the

gantry rotation. This is another unique feature of this system that allows for the treatment of peripheral tumors such as breast or lung tumors.

1.3 Motivation

The main components of the biplanar magnet for the Linac-MR system are yoke, pole plates, and superconducting coils. The yoke is a ferromagnetic structure that supports the magnet poles, and carries the magnetic flux around the system. Critical to the success of the biplanar Linac-MR system is the design of a magnetic yoke structure that allows for a homogeneous magnetic field over a large field of view. Magnetic field homogeneity allows for artifact-free imaging and accurate geometrical information of the target volume during the treatment. In addition to the stringent requirements on the magnetic field uniformity for the image quality, there are other criteria that are imposed on the system due to the unusual circumstances in which the MR imager must operate. Specifically, the yoke should be designed to have ample patient access, and to be sufficiently compact to rotate in a typical clinical vault. In addition, it must allow room for the linac assembly to be positioned within a limited distance from the isocentre of the device.

The biplanar MR radiotherapy hybrid as being developed by our group[(17)], has an increased SAD compared to the 100 cm standard, mainly due to the position of the linac, which must be outside the yoke and in a low magnetic field zone. The latest system has an SAD of 130 cm[(18)], where the radiation beam is parallel to the direction of magnetic field. This increase in SAD

will cause the reduction of the dose rate at the isocentre by 41% due to the inverse square law, with potential consequences for patient treatment times. Consequently, the reduction of this SAD will be a valuable objective of any new design.

Conventionally, bi-planar superconducting magnets have the coils placed axially adjacent to the pole plates to produce the desired magnetic field[17;28]. The coils are enveloped by a bulky cryostat, which extends on the order of 30 cm or more in the vertical dimension. For the new design, the superconducting current loops are moved to surround the yoke supports that connect the pole plates. This non-axial design is reminiscent of a C-core transformer. The intention in this new design is to reposition as many structures that are currently between the patient and the linac as possible. Moving the coils to the side allows for reduced SAD while improving the patient access, which is important to reduce patient claustrophobia and clinician access.

One of the primary functions of the Linac-MR system is tracking tumors. For the new design, target field for the homogeneity is considered to be an ellipsoid versus a sphere, which is the common practice for designing a magnet. This allows a wider field-of-view in lateral direction that increases the accuracy for the patient set-up. Once the gantry is rotated, PTTP method[29] is applied to keep the tumor in the axis of the beam, where an accurate small field-of-view is required for tracking the tumor. However, the target volume might be located anywhere along the beam axis.

This work presents the development of a unique non-axial superconducting

biplanar magnet design as a proof of concept. Moving the coils to the yoke support allows for a minimal SAD and improved patient access, which are the distinct features of this design. Using a finite-element analysis technique, the shape of the pole plate for the magnet assembly is optimized to achieve the desired field uniformity over a field-of-view suitable for MR imaging.

1.4 Thesis Outline

The outline of this thesis is as follows:

A review on the design of an MR magnet is given in chapter 2. In addition, the mathematical tools applied for this work are introduced. A brief description on the finite-element procedure is provided, then the application of the method in a magnetostatic model is explained. Finally, the optimization algorithms used for the optimization of the pole plate design are described.

Chapter 3 builds on investigations of two simplified designs in order to find the proper optimization algorithm and pole plate structure for a final non-axial design. The symmetrical magnet assemblies are the tapered conical projections model and the continuous cylindrical projections model. The technique evaluation, using the closed models with no patient access, leads to the final design. The shape of the pole plate for this design is then optimized. The magnetic field calculations required for this work were performed with the 3D finite element method (FEM) software package, Opera-3D[(30)]. The design features and optimization results are explained in chapter 4.

Chapter 5 summarizes and presents conclusion on this work, and suggests the direction for future work.

Chapter 2

Background

2.1 Magnetic Resonance Imaging

The basic principles of magnetic resonance (MR) imaging can be related to the roles of different types of magnetic fields. The MR scanner has three main components to generate images: the main magnet is used to generate a static and highly uniform magnetic field (B_o), radio frequency (RF) coils are used to generate a time varying magnetic field (B_1), and gradient coils are used to generate a highly linear magnetic field that can be turned on and off in a time-varying fashion[31]. The purpose of this section is to briefly review the function of each magnetic field at different stages of imaging, using the physical principles of MR imaging.

2.1.1 Static Magnetic Field

Most atomic nuclei have intrinsic quantum mechanical properties including non-zero spin (angular momentum) and a charge distribution. A charged particle with angular momentum can be modeled as an electrical current loop creating a magnetic moment μ expressed as:

$$\mu = \gamma \hbar I, \tag{2.1}$$

where $\hbar I$ is the angular momentum of the nucleus and γ is a constant called the gyromagnetic ratio with its value depending on the element nucleus[32]. The most common nucleus targeted for MR imaging is the hydrogen (^1H) nucleus (proton) due to its abundance in the human body. It has I equal to $\pm 1/2$ and γ equal to 2.675×10^8 rad s^{-1} T^{-1}. From here on, the system of protons will be used to explain the MR imaging process.

When a proton is placed in a strong external magnetic field B_o, the proton experiences a torque τ given by:

$$\tau = \mu \times B_o. \tag{2.2}$$

The torque causes precession of the proton's magnetic moment with an angular frequency proportional to the magnetic field strength. The precessional frequency is called the Larmor frequency and is defined by the following equation:

$$f_o = \frac{\gamma}{2\pi} B_o. \tag{2.3}$$

The proton can occupy two stable energy states, either spin-up ($I = 1/2$, lower energy state) or spin-down ($I = -1/2$, higher energy state), which can be explained by the use of quantum mechanics[33]. The proton will be aligned either parallel or anti-parallel to B_o for the low or high energy state, respectively. It can be shown that there is slightly greater number of protons in the parallel direction[33]. Therefore, an ensemble of protons precessing at thermal equilibrium about B_o, oriented in the longitudinal direction (z-axis) generates a net static magnetization oriented in the z-direction and no net magnetization in the transverse plane (xy-plane). As a result, there is no detectable RF signal at this stage and the net magnetization needs to be manipulated to produce a measurable signal.

2.1.2 Radio Frequency Magnetic Field

The system of protons must be perturbed to produce a detectable signal and create an MR image. This can be done by applying an RF magnetic field (B_1) with a frequency equal to the Larmor frequency (f_o) and perpendicular to B_o. When enough energy is supplied using an RF pulse the net longitudinal magnetization is tipped toward the transverse plane. The displacement of the magnetization vector from the z-direction can be measured by an angle called flip angle (α), which depends on the duration that the RF pulse is applied. For $\alpha = 90^o$, the net magnetization (M) is projected onto the transverse plane with no component in z-direction. This is called a full saturation. In addition, the magnetization direction can be inverted if the RF pulse is applied with flip angle of 180^o[34].

After tipping M toward the transverse plane, the transverse component (M_T) rotates about B_o due to the nuclear precession. Therefore, the M_T vector has a circular motion in the transverse plane, and creates a detectable signal.

The detectable signal decays due to two types of nuclear relaxations. The first one is the spin-lattice relaxation due to the interaction of the spin with the surrounding medium, and tends to cause recovery of the M_z component. The time for spin-lattice relaxation is characterized by T_1. The second mode of relaxation can be explained in term of the spin-spin interactions, which creates additional dephasing. This causes decay of the M_T component and it is characterized by the relaxation time T_2. The resultant decaying signal is called free induction decay (FID). The mathematical description of the M_z recovery and the M_T decay can be understood using the Bloch equations[35]:

$$M_z = M_o - (M_o - M_z(0)) \left(1 - e^{-\frac{t}{T_1}}\right), \tag{2.4a}$$

$$|M_T| = |M_T(0)|\, e^{-\frac{t}{T_2}}, \tag{2.4b}$$

where $M_z(0)$ is the value of M_z immediately after applying a RF pulse, and ranges from $-M_o$ to M_o. $M_T(0)$ is the value of M_T right after applying a RF pulse, and ranges from 0 to M_o. The final signal intensity depends on the proton density, the recovery of the M_z, and the decay of the M_T.

The main function of RF coils, which produce the RF magnetic field, is to excite the magnetization. However, they are also used to receive the signal created by the excited magnetization.

The T_2 relaxation time is always shorter than T_1, for any given tissue. In addition, T_1 and T_2 have different values in various tissues for different magnetic field strengths. These characteristics provide a range of possible contrast mechanisms to generate an image using an MR scanner.

2.1.3 Gradient Magnetic Field

Using the primary and RF magnetic fields alone, all spins in an ensemble of protons resonate at the same frequency, are excited, and produce a signal with no spatial information. Spatial localization in a 3D volume can be done using three gradient magnetic fields in three steps: slice selection, frequency encoding, and phase encoding. The gradient magnetic fields can be defined as additions to the main magnetic field, B_o, with the following equation:

$$B_z(x, y, z, t) = B_o + xG_x(t) + yG_y(t) + zG_z(t). \tag{2.5}$$

The field gradients, G_x, G_y, and G_z, are often expressed in units of millitesla per meter (mT m^{-1}). They are designed such that the center of an imaging volume is located at $x = y = z = 0$. Then, the gradient magnetic fields vary linearly with the position and can be controlled independently[35].

The first step for spatial localization is slice selection. Applying a gradient field results in having different magnetic fields at different spatial locations. Therefore, protons at different locations resonate with different Larmor frequencies. In order to excite M and produce a signal, the frequency of the RF

pulse must match the Larmor frequency. To select a single slice, the frequency bandwidth of B_1 must match the bandwidth of the resonance frequencies of the spins in the slice of interest. The frequency bandwidth, $\Delta\omega_z$, is defined as:

$$\Delta\omega_z = \gamma z G_z. \tag{2.6}$$

In order to select a transverse slice, a gradient field must be applied in the z-direction, parallel to B_o. Based on (2.6), the slice thickness depends on the bandwidth of the RF pulse and the gradient strength.

The frequency encoding gradient is applied in a direction perpendicular to the direction of the slice selection gradient, which is the x or y-direction in the case of transverse slice selection. Frequency encoding works in the same way as slice selection, but the gradient is applied during signal acquisition. Assuming a gradient field applied in the x-direction, the protons at different x-positions precess with the frequencies determined by their position from the center of the imaging volume. From each x-position, a signal is emitted with the frequency determined by the x location and an amplitude dependent on the number of protons at the location. The composite signal detected by a receiver coil results from the sum over all individual signals. The composite signal is decoded by use of a Fourier transform to recover the position information[(33)].

The last step in spatial localization of a signal is phase encoding. The gradient field for phase encoding is applied after the slice selection gradient, before the

frequency encoding gradient, and in the direction of the third perpendicular axis (y). Turning on the phase encoding gradient results in the variation of the precessional frequency in the y-direction; similar to the last two steps. After turning off the gradient, the different precessional frequencies are translated into phase differences. Assuming that the phase encoding gradient at location y is on for a finite time τ, the phase difference (ϕ_y) can be defined as:

$$\phi_y = -\gamma y \int_0^{\tau} G_y(t')\ dt'. \tag{2.7}$$

For N_y sampling points in the y-direction, the phase of the signal is changed and expressed by ϕ_1 to ϕ_{N_y} for each point. After applying the frequency encoding for N_x sampling points, the frequency as a function of position in x-direction is expressed by f_1 to f_{N_x}. Therefore, N_x data points are derived after a single acquisition, and phase encoding gradients with different strengths must be applied N_y times to fully encode the image[35].

2.2 Primary Magnet Design

The main magnet in a MR scanner is used to produce a static and homogenous field throughout the scan. The magnetic field makes nuclear spins align parallel to B_o, which induces a net longitudinal magnetization and precession. To design an optimal magnet, one needs to thoroughly understand the required characteristics for the main magnet.

2.2.1 Required Features for Main Magnets

Characteristics that might be considered when designing a magnet include: the main field strength, temporal stability of the field, minimization of the fringe field, field homogeneity, patient access and comfort, and cost effectiveness[32].

Main Field Strength and Temporal Stability

The strength of the net magnetization, which is directly related to the received signal, is dependent on the B_o field strength[35]. In addition, the signal-to-noise ratio (SNR), defined as the ratio between the signal and background noise, is roughly proportional to B_o. For higher fields, there is a direct proportionality between the SNR and B_o. However, the noise dynamic changes and the SNR begins to drop more rapidly with B_o when the field strength is roughly below a threshold of 0.5 T[32].

The signals produced to obtain MR images are acquired over a scan time, through successive excitations of spin magnetization in the object. As the term static magnetic field implies, the field should be time-independent during imaging. The temporal stability is dependent on the magnet type and design.

Fringe Field Minimization

The magnetic field produced by the main magnet, but outside the imaging environment, is called the fringe field. The fringe field should be kept below 5 G in public areas to avoid any safety risks to people as 5 G has been generally established as safe for the vast majority of implant devices. The fringe field strength depends on the magnet type and its field strength. Any excessive field may interact with magnetic materials and sensitive electronic devices that are in the vicinity of the MR scanner, which is hazardous.

For unshielded magnets, producing field about 0.5 T and above, the fringe field can be more than 5 G at distances of 10 to 30 m from the imaging environment[32]. Therefore, in order to minimize the effect of fringe fields, shielding strategies should be considered when a magnet is designed. Two types of shielding approaches can be employed: active shielding and passive shielding.

In the active shielding approach, there are two sets of coils. The primary set produces the B_o field, while the exterior secondary one set produces currents in the opposite direction. This design helps to keep the magnetic flux in a smaller region and reduce the fringe fields.

In the case of passive shielding, ferromagnetic materials with high magnetic permeability (μ) (such as steel) are employed in two ways. Firstly, after installing an unshielded magnet, steel materials are added to the wall of an

imaging room. The presence of the iron lets some of the excess flux pass through the shield, reducing the fringe field extending outside the room. In an alternative approach, inclusion of the ferromagnetic material is considered at the design stage. The primary source producing B_o is surrounded by a large magnetic yoke structure, which contains the field lines and results in reduced fringe fields.

Main Magnet Field Homogeneity

The required homogeneity of B_o varies based on the objective of the MR imaging studies being performed and the imaging methodologies being used. The homogeneity of the main field is quoted in terms of inhomogeneity, which is defined by ΔB over the region of interest. It can be expressed in parts per million (ppm) as:

$$\Delta B = max\left(\left|\frac{B(\overrightarrow{\mathbf{r}}) - B_o}{B_o} \times 10^6\right|\right), \tag{2.8}$$

where $B(\overrightarrow{\mathbf{r}})$ is the magnetic flux value at the point $\overrightarrow{\mathbf{r}}$ positioned at the region of interest. Main field inhomogeneity results in geometric distortion and signal loss.

As mentioned before, the Larmor frequency is linearly dependent on B_o. When a linear gradient is applied to encode the location of a spin, any field variations (ΔB) are added to the applied linear field gradient, which leads to a deviation from the intended frequency of precession for the given spin. Consequently, the actual location of the spin is misregistered, and the spatial

distortion resulting from the inhomogeneity is given by[32]:

$$\Delta x = \frac{\Delta B}{G_x}. \tag{2.9}$$

In addition to geometric distortion, the relaxation due to the decay of the transverse magnetization in the presence of field inhomogeneity is defined as:

$$\frac{1}{T_2^*} = \frac{1}{T_2} + \frac{1}{\Delta B}, \tag{2.10}$$

where ΔB is the variation in the B_o field[35]. Consequently, the rate of signal decay is faster when there is an inhomogeneity in the syetem.

There are multiple factors that leads to the magnetic field inhomogeneity after magnet installation. There are always inaccuracies in magnet manufacturing such as machine error during the magnet fabrication or magnetic impurities in any of the surrounding structures[35]. In addition, the presence of steel materials in the building might contribute to magnetic field inhomogeneity after magnet installation. The process of assessing these inhomogeneities and applying different methods to eliminate them is referred to as shimming.

The solution of Laplace equation ($\bigtriangledown^2 B_z = 0$) in spherical coordinates can describe the magnetic field distribution within a volume with no currents, where B_z is the component of the magnetic field in z-direction (more details on electromagnetics will be described in the following section). This solution can be expressed in terms of spherical harmonic functions[36;37], and the concept can be used in the shimming process.

Upon installation of a magnet, the magnetic field homogeneity is assessed using field mapping. The field distribution, within the imaging volume of a magnet, is determined using a field probe (consisting of a small nuclear magnetic resonance (NMR) coil and sample) to measure the Larmor frequencies at points defined within the sample. The probe is typically moved over the outside of a volume (the surface of a sphere or cylindar). The measured magnetic field can be expanded as a sum of weighted spherical harmonic components. Using a computer algorithm, the coefficient of each spherical harmonic term is calculated. Each coefficient determines the residual inhomogeneity associated with the corresponding spherical harmonic[38]. The next step is to determine a magnetic source configuration to generate the spherical harmonic solution that can eliminate the residual inhomogeneity[36]. The process requires several iterations of measurement and correction to obtain desirable homogeneity. Similar to the approaches applied for the magnet shielding, there are active and passive shimming methods for the main magnet. For passive shimming, magnetic materials are placed in the magnet bore to compensate for unwanted spherical harmonic components, and for active shimming, a set of shim coils is added to the magnet to cancel the extra fields.

2.2.2 Superconducting Magnet

There are three types of magnets: permanent magnets, resistive magnets, and superconducting magnets. The superconducting magnets have several advantages when requirements of the magnet design are taken into consideration.

From the field strength point of view, it is difficult to achieve fields for whole body above $0.2 - 0.3$ T with permanant magnets, and the resistive one typically operates in $0.3 - 0.5$ T[31]. The magnetic field generated by a wire is linearly proportional to the current within the wire. Superconducting materials can carry much larger current compared to the resistive one. Therefore, the superconducting conductor can generate higher B_o, given a constant number of windings. There are commercially available superconducting human whole body systems with a B_o of 7 T.

Considering temporal stability, permanent magnets are quite sensitive to temperature fluctuation, and a special system for temperature monitoring and regulation are generally required for this system. The resistive magnets require a highly stable power supply and cooling system to reduce magnetic field variations that might occur during the scanning session. This adds cost to the system. However, the variation in field for superconducting magnets is typically less (on the order of $\mu T/hour$), and generally small enough to neglect for imaging purposes[32].

The characteristics of a superconducting material is determined by its critical temperature, critical magnetic field strength, and critical electrical current. The superconductor must operate at a temperature or current below the critical parameters to achieve zero electrical resistance.

Currently, niobium-titanium (NbTi) with a maximum critical temperature of 9.5 ^{o}K[31] is the most popular superconducting material used in super-

conductor magnets. The operating temperature for these magnets is kept at 4.2 ^{o}K, which is the temperature of liquid helium. Coils are submerged in a liquid helium tank by an auxiliary cryostat vessel. However, there is an increasing interest in using high-temperature superconducting (HTS) materials such as MgB_2, which has a maximum critical temperature of 39 ^{o}K[39]. These superconductors can be employed as conduction-cooled superconductor magnets[40], which is free of liquid cryogens. This greatly reduces the complexity of the systems.

2.3 Finite Element Method

The Finite Element Method (FEM) is based on the idea of discretization of a continuous system to provide an approximate numerical solution for a boundary value problem. A detailed description have been published in[41;42]. The method is widely used to find an approximate solution for problems in engineering and physics that are defined by the general differential equation:

$$\mathcal{L}u = f, \tag{2.11}$$

where $\mathcal{L}$ is a differential operator and f is the forcing (source) function. u is the unknown solution that one is looking for on a domain Ω and boundary Γ, with defined boundary conditions.

The method is formalized through four major steps that convert the differential equation, defined on a continuous and geometrically complicated domain,

into a set of linear equations that can be solved numerically. The steps include: (i) the subdivision of the solution domain, (ii) selection of the finite element basis functions, (iii) forming the system of linear equations via elemental equations, and (iv) solving the system of equations numerically. The steps are explained in more detail in the following sections.

2.3.1 Domain Subdivision

The first step is dividing the domain Ω into a finite number, m, of subdomains Ω^e $(e = 1, 2, 3, ..., m)$. Each subdomain is called an element and the vertices of each element are called nodes. The common types of the elements for problems in different dimensions is illustrated in figure (2.1). The triangular and tetrahedral elements are commonly used for two-dimensional surfaces and three-dimensional volumes with the irregular geometries. Potential errors in the model can be minimized using these elements[41]. Using elements with right angles leads to unavoidable errors due to the nonconformity of the elements to the true geometry.

To fill the whole domain properly (mesh generation) two adjacent elements should be connected at their vertices, where no gaps and overlaps are permitted. Mesh generation can be optimized using the Delauney triangulation algorithm[42], while satisfying the mesh generation requirements.

To implement the FEM, one needs to have information for all the nodes, which includes the local number (indicating position of the node within an

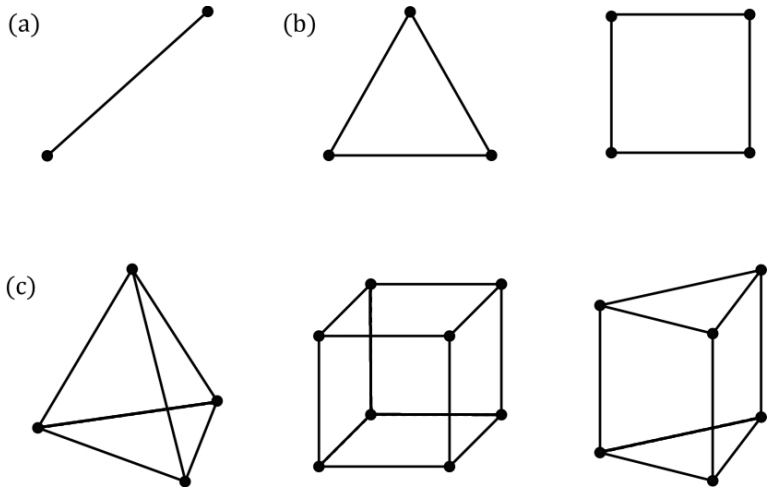

Figure 2.1: Common elements (a) one-dimensional problem, (b) two-dimensional problem, (c) three-dimensional problem; figures taken from[41].

element), the global number (indicating position of the node in the whole domain), and the coordinates for each node[43]. The index number, $n(e,i)$, relates the local number (i) for an element (e) to its global number (n). i runs from 1 to j, where j is the number of nodes in the element. The global number runs from 1 to N, where N is the total number of the nodes in the domain. Using this information, an element connectivity matrix is formed to map the local node numbers to the global node numbers, with the dimensions of $N \times N$. A similar connectivity matrix is formed for the boundary nodes to relate the local and the global nodes for the boundary surface with a defined boundary condition. Another matrix is formed including the coordinates for each node. These matrices are used to calculate the elemental equations and matrix assembly for the next steps. The domain subdivision is considered a preprocessing step because it can be done independently from the other steps[41].

2.3.2 Selection of the Finite Element Basis Functions

After the domain is discretized properly, one needs to find an approximation to the function u using interpolating functions within each element (u^e). The approximation function, $\widetilde{u}$, is defined as:

$$\widetilde{u} = \sum_{e=1}^{m} u^e, \tag{2.12}$$

where m is the total number of elements, and u^e is the basis function. The most common basis functions are the Lagrange polynomials. The higher-order polynomials are the most accurate approximation. However, the linear and quadratic polynomials were used in this thesis due to the simplicity.

The polynomial basis function must be complete, which means it should allow for all combinations of the coordinate variables defined as $x^i y^j z^k$, where $0 \leq i + j + k \leq q$ for polynomials of order q. As a result, one has $n = \frac{1}{6}(q+1)(q+2)(q+3)^{(41)}$ terms with n unknown coefficients. Therefore, n nodes are needed for each element to uniquely determine the unknown coefficients.

To calculate the unknown coefficients, a system of equations can be defined in terms of coordinates and the values of u at the n^{th} nodal points for the element e. Taking this into account, the basis function u^e can be expressed

in the following form as:

$$u^e(x, y, z) = \sum_{i=1}^{n} u_i^e \ \lambda_i^e(x, y, z), \tag{2.13}$$

where n is the number of the nodes in the element e and u_i^e is the value of u at the nodal point i of element e with coordinate $(x_i,\ y_i,\ z_i)$. λ_i^e is the basis function for the element e and node i, which is a polynomial of the order q.

The basis function λ_i^e has a value of one for node i, and zero for the rest of the nodes. These properties of the basis function can be summarized in the following equation:

$$\lambda_i^e(x_j, y_j, z_j) = \delta_{ij}. \tag{2.14}$$

The other important property of λ_i^e is that it has compact support, which means it is nonzero only within the element e.

For a Lagrangian tetrahedral element, the volume coordinate, also known as Barycentric coordinate, is introduced to define the basis function λ_i^e. The volume coordinate is a local coordinate, which is formulated using $L_i^e(x, y, z)$ with the following definition:

$$L_i^e(x, y, z) = \frac{V_i(x, y, z)}{V^e}, \tag{2.15}$$

where V^e is the volume of the element e and $V_i(x, y, z)$ is defined as the volume of the sub-tetrahedral element when the nodal point i is replaced by point P with coordinate $(x,\ y,\ z)$. A tetrahedral element and sub-tetrahedrons,

formed by replacing each point of the main element with an arbitrary point P, are shown in (2.2).

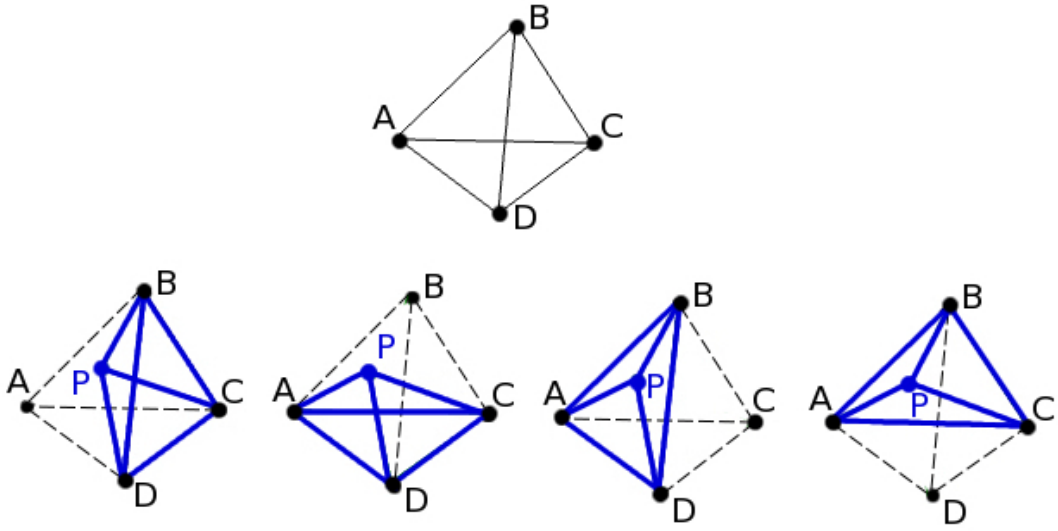

Figure 2.2: Top row: tetrahedral element ABCD. Bottom row: sub-tetrahedrons formed by replacing each point of the main element A, B, C, and D with P, respectively.

Using the volume coordinate, the node i located at (x_i, y_i, z_i) can be labeled as (k_1, k_2, k_3, k_4) with the following definition for k_j:

$$k_j = q\ L_j^e(x_i, y_i, z_i), \tag{2.16}$$

where q is the order of the polynomial. Considering the volume coordinate and nodal labels, λ_i^e can be formulated as[42]:

$$\lambda_i^e(x, y, z) = l_{k_1}^q(L_1^e)\ l_{k_2}^q(L_2^e)\ l_{k_3}^q(L_3^e)\ l_{k_4}^q(L_4^e), \tag{2.17}$$

for $L_i^e = L_i^e(x, y, z)$ and $l_{k_i}^q(L_i^e)$ is defined as:

$$l_{k_i}^q(L_i^e) = \frac{1}{k_i!}\prod_{j=0}^{k_i-1}(qL_i^e - j), \tag{2.18}$$

with $l_0^q(L_i^e) = 0$. It can be verified that the basis function (λ_i^e) defined by (2.17) satisfies the properties summarized in (2.14) and $\sum_{i=1}^{n} \lambda_i^e = 1$.

For two dimensions, the triangle can be used as the element for the mesh generation. A similar formulation can be used for this case by adjusting the equations for two dimensions. The area coordinate known as Barycentric coordinate system is employed to define the basis functions. An example of a two-dimensional element to determine basis functions is given in Appendix A.

For the complex geometries, one must address the irregular boundaries. In order to have an accurate approximation for the elements with the curved boundaries, one can transform the curved element in xyz-space to a regular element in $\xi\eta\zeta$-space, shown in figure (2.3). The transformation can be described as:

$$x(\xi, \eta, \zeta) = \sum_{i=1}^{n} \lambda_i^e(\xi, \eta, \zeta)\, x_i, \tag{2.19a}$$

$$y(\xi, \eta, \zeta) = \sum_{i=1}^{n} \lambda_i^e(\xi, \eta, \zeta)\, y_i, \tag{2.19b}$$

$$z(\xi, \eta, \zeta) = \sum_{i=1}^{n} \lambda_i^e(\xi, \eta, \zeta)\, z_i, \tag{2.19c}$$

where n is the number of the nodes for the element e. x_i, y_i, and z_i indicate the position of the i^{th} node of the curved element in xyz-space. It can be shown that the λ_i^e is given by[41]:

$$\lambda_i^e(\xi,\eta,\zeta) = l_{k_1}^q(1-\xi-\eta-\zeta)\ l_{k_2}^q(\xi)\ l_{k_3}^q(\eta)\ l_{k_4}^q(\zeta), \tag{2.20}$$

where $l_{k_i}^k$ has the same definition as (2.18). The transformed λ_i^e is called the shape function. When the order of the polynomial in the shape function and the basis function are the same, the transformed elements are called isoparametric elements.

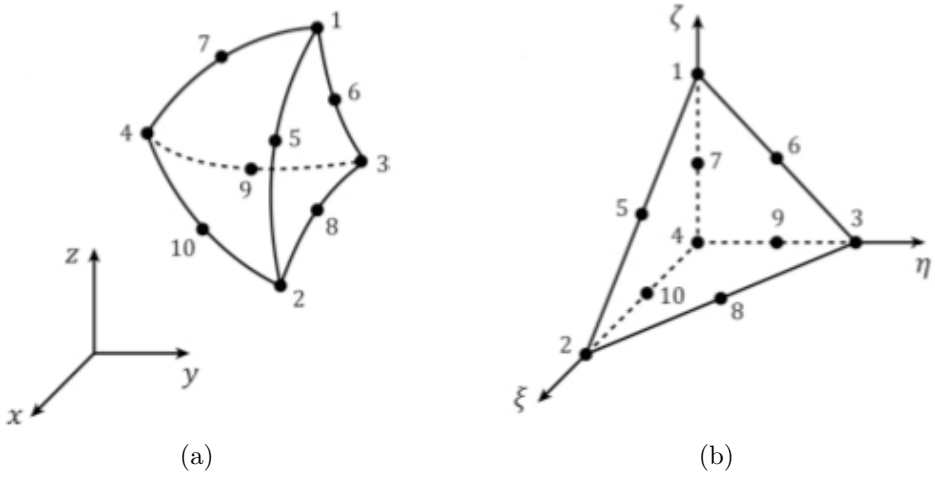

(a) (b)

Figure 2.3: (a)A tetrahedron in curved space. (b) The transformed tetrahedron in the cartesian space; figures taken from[41].

2.3.3 Galerkin-Weighted Residual Approach

After discretizing the whole domain, the approximation of the exact solution for (2.11) is expressed using the basis functions defined by (2.13). The basis

functions are formed by a set of linearly independent functions defined locally for each element e. A quantity called the residual (R) is defined as:

$$R = \mathcal{L}\tilde{u} - f. \tag{2.21}$$

The value of R is zero for the exact solution. To find the approximation function ($\tilde{u}$), a scheme must be set-up to make the residual small over the whole domain using the nodal values u_i^e and the basis functions λ_i^e for each element. There are different approaches to find the minimum value of the residual such as least squares, variational methods, and weighted residual. The most common method is the weighted residual, where a weighted integral is introduced as:

$$R_i^e = \int_{\Omega^e} w_i^e \ (\mathcal{L}u^e - f) \ d\Omega^e. \tag{2.22}$$

w_i^e is the selected weight and Ω^e is the domain for element e. To determine the unknown coefficients, R_i^e is forced to be zero. When the selected weight is chosen to be the same as the basis function, $w_i^e = \lambda_i^e$, the method is called the Galerkin method. Therefore, the weighted residual for each element is:

$$R_i^e = \int_{\Omega^e} \lambda_i^e \ (\mathcal{L}u^e - f) \ d\Omega^e. \tag{2.23}$$

One can apply (2.23) to a general form of the partial equation with the differential operator L defined as $\bigtriangledown \cdot \alpha \bigtriangledown$. Considering that the goal is to make

R_i^e become close to zero, one has:

$$\int_{\Omega^e} \lambda_i^e \ (\bigtriangledown \cdot \alpha \bigtriangledown u^e) \ d\Omega^e - \int_{\Omega^e} \lambda_i^e \ f \ d\Omega^e = 0. \tag{2.24}$$

Applying integration by parts for the first term of (2.24) gives:

$$\int_{\Omega^e} \bigtriangledown \lambda_i^e \ \cdot \alpha \bigtriangledown u^e \ d\Omega^e - \int_{\Gamma^e} \lambda_i^e \ \alpha \bigtriangledown u^e \ \cdot dn - \int_{\Omega^e} \lambda_i^e \ f \ d\Omega^e = 0. \tag{2.25}$$

For internal elements, the second integral is zero since the normal vector for the common surface of two adjacent elements are in opposite directions and the basis functions are the same, therefore they cancel each other for the final matrix assembly. For the boundary elements, the second integral can be calculated based on the boundary condition for the boundary element to determine the nodal value for that element.

Using (2.12) and (2.13), the matrix form of (2.25) is obtained as $Ku = F$ with the following definitions for K, u, and F:

$$\sum_{j=1}^{m} u_j \underbrace{\sum_{e=1}^{m} \overbrace{\int_{\Omega^e} \bigtriangledown \lambda_i^e \ \cdot \alpha \bigtriangledown \lambda_j^e \ d\Omega^e}^{K_{ij}^e}}_{K_{ij}} = \underbrace{\sum_{e=1}^{m} \overbrace{\int_{\Omega^e} f \lambda_j^e \ d\Omega^e}^{F_i^e}}_{F_i}, \quad i = 1, 2, ..., m. \tag{2.26}$$

The matrices K and F are known as the stiffness matrix and the load matrix respectively. The integrals for (2.26) are calculated analytically for simple cases, or numerically using Gauss-Legendre quadrature[41]. Summation over the elemental equation (2.26) and forming the stiffness and load matrices using the element connectivity matrix is considered as the matrix assembly

process for FEM.

With the system of equations in the matrix form, the final step is to solve the equation: $Ku = F$. Having the basis function for the weight function, the matrix K is a sparse matrix[44]. There are a variety of methods to solve this system of equations, mentioned in[41]. The Opera-3D[30], FEM software package, applies the Newton-Raphson method - a suitable method for a nonlinear problem in electromagnetics.

2.4 Finite Element Method in Electromagnetics

The evaluation of electromagnetic fields is a crucial part of the design process for different devices. The problem is defined by the partial differential equations derived from Maxwell's equations with appropriate boundary conditions. The electromagnetic field simulation for the complicated geometries of such devices should be done accurately. The FEM is one of the approaches used to do numerical analysis for the electromagnetic field calculations.

2.4.1 Maxwell's Equations

Maxwell's equations describe the relation between the electromagnetic field and the source of the electromagnetic field. The mathematical description of electromagnetic fields is formulated by Maxwell's equation in differential form

as[45]:

$$\bigtriangledown \cdot \mathbf{D} = \rho, \tag{2.27a}$$

$$\bigtriangledown \times \mathbf{E} = -\frac{\partial \mathbf{B}}{\partial t}, \tag{2.27b}$$

$$\bigtriangledown \cdot \mathbf{B} = 0, \tag{2.27c}$$

$$\bigtriangledown \times \mathbf{H} = \mathbf{J} + \frac{\partial \mathbf{D}}{\partial \mathbf{t}}, \tag{2.27d}$$

where **E**, **H**, **D**, and **B** are the electric field intensity, the magnetic field intensity, the electric flux density, and the magnetic flux density respectively. The sources of the electromagnetic field are electric current density **J** and the electric charge density ρ. The field quantities are not independent and are described by the following equations called constitutive relations:

$$\mathbf{D} = \varepsilon \mathbf{E}, \tag{2.28a}$$

$$\mathbf{B} = \mu \mathbf{H}, \tag{2.28b}$$

where ε is the permittivity and μ is the permeability of the medium through which the electromagnetic fields propagate.

2.4.2 Magnetostatics Problems

The fields are independent of time for the magnetostatics case. Therefore, the following set of Maxwell's equations can describe this case:

$$\bigtriangledown \cdot \mathbf{B} = 0, \tag{2.29a}$$

$$\bigtriangledown \times \mathbf{H} = \mathbf{J}. \tag{2.29b}$$

The magnetic field intensity, $\mathbf{H}$, can be split into two parts: $\mathbf{H}_s$ and $\mathbf{H}_m$ [46;47]. $\mathbf{H}_s$ is the magnetic field produced by the current source $\mathbf{J}$, which is contained in the region Ω_j, and $\mathbf{H}_m$ is the rest of the field. Let $\bigtriangledown \times \mathbf{H}_m = 0$, H_m can be derived using the scalar potential ϕ as:

$$\mathbf{H}_m = - \bigtriangledown \phi. \tag{2.30}$$

Using the Biot−Savart law, $\mathbf{H}_s$ can be derived as:

$$\mathbf{H}_s = \frac{1}{4\pi} \int_{\Omega_j} \frac{\mathbf{J}(\mathbf{r}_j) \times (\mathbf{r} - \mathbf{r}_j)}{|(\mathbf{r} - \mathbf{r}_j)|^3} \, d\Omega_j, \tag{2.31}$$

where $\mathbf{r}_j$ is the source point and $\mathbf{r}$ is the field point. The integral (2.31) can be calculated numerically using Gauss-Legendre quadrature [30].

The magnetic field intensity is defined as:

$$\mathbf{H} = - \bigtriangledown \phi + \frac{1}{4\pi} \int_{\Omega_j} \frac{\mathbf{J}(\mathbf{r}_j) \times (\mathbf{r} - \mathbf{r}_j)}{|(\mathbf{r} - \mathbf{r}_j)|^3} \, d\Omega_j. \tag{2.32}$$

Divergence of the magnetic flux density is always zero and the magnetic flux density can be related to the magnetic field intensity using (2.28b). Therefore, the final partial equation is summarized as:

$$\bigtriangledown \cdot \mu(\mathbf{r}) \bigtriangledown \phi(\mathbf{r}) = \bigtriangledown \cdot \left(\frac{\mu(\mathbf{r})}{4\pi} \int_{\Omega_j} \frac{\mathbf{J}(\mathbf{r}_j) \times (\mathbf{r} - \mathbf{r}_j)}{|(\mathbf{r} - \mathbf{r}_j)|^3} \, d\Omega_j \right). \tag{2.33}$$

Equation (2.33) is a nonlinear Poisson type equation and the scalar potential field, ϕ, is called the reduced scalar potential.

In the case of a material with high permeability, the numerical results from (2.33) have been shown to be inaccurate compared to the analytical calculation in the region containing materials with high permeability[46]. Inside the magnetic material, the values of $\mathbf{H}_s$ (field from the known source) and $\mathbf{H}_m$ (field from the calculated potential field) tend towards being equal and opposite, i.e. $\mathbf{H}_s \approx \bigtriangledown\phi$. This causes loss of precision as two separately-computed parts cancel each other[47]. This is called the cancellation error in numerical calculations, which occurs when the error in the fields calculation dominates the difference between $\mathbf{H}_s$ and $\bigtriangledown\phi$[46].

The two-scalar potential formulation is introduced to apply for the case with high permeability material[46;47]. The problem's region is divided into two regions: one includes all the currents, Ω_2, and one that includes the material with high permeability and no currents, Ω_1. Equation (2.33) is used to find the scalar potential for Ω_2. For Ω_1, a scalar potential ψ is derived using:

$$\bigtriangledown \cdot \mu \bigtriangledown \psi = 0, \tag{2.34}$$

where equation (2.29b) holds with $\mathbf{J} = 0$ and ψ is called the total scalar potential. This equation is the non-linear Laplace equation.

The FEM can be implemented to do the magnetostatic analysis by using

(2.33) and (2.34), when the problem includes the high permeability material. The vector F, defined in (2.26), is zero for region Ω_1 and it is equal to $\bigtriangledown \cdot \mathbf{H}_s$ for region Ω_2. Then, the solutions must be coupled at the interface between two regions. Therefore, an extra boundary condition should be applied for the nodes located at the interface of two regions as illustrated in figure (2.4).

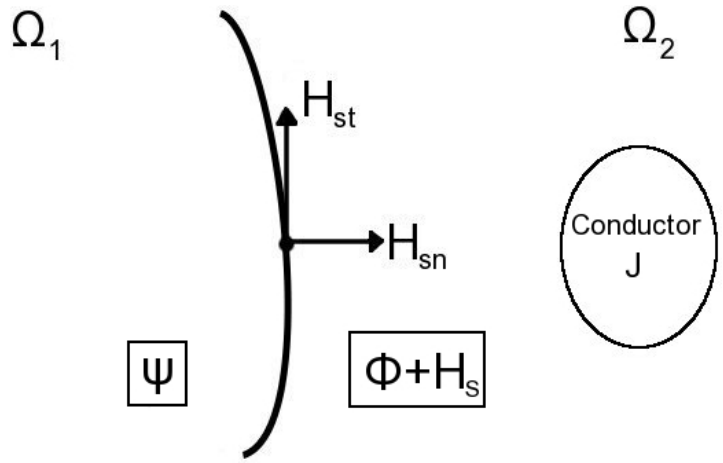

Figure 2.4: Interface between two regions and corresponding scalar potentials.

The vector fields should be continuous at the interface of different materials, thus the limiting forms of equations (2.29a) and (2.29b) give the interface conditions as:

$$(\mathbf{B}_2 - \mathbf{B}_1) \cdot \mathbf{n} = 0, \tag{2.35a}$$

$$(\mathbf{H}_2 - \mathbf{H}_1) \times \mathbf{n} = 0. \tag{2.35b}$$

Applying the continuity equations (2.35a) and (2.35b) at the interface of the magnetostatic problem gives:

$$-\mu_1 \frac{\partial \psi}{\partial n} \Big|_{\Omega_1} = \mu_2 (-\frac{\partial \phi}{\partial n} + \mathbf{H}_{sn}) \Big|_{\Omega_2}, \tag{2.36a}$$

$$-\frac{\partial \psi}{\partial t} \Big|_{\Omega_1} = -\frac{\partial \phi}{\partial t} + \mathbf{H}_{st} \Big|_{\Omega_2}, \tag{2.36b}$$

where $\mathbf{n}$ is the normal vector and $\mathbf{t}$ is the tangential vector at the interface. $\mathbf{H}_{sn}$ is the normal component of $\mathbf{H}_s$, and $\mathbf{H}_{st}$ is the tangential component of $\mathbf{H}_s$. The integral form of the second condition can be derived by integration of (2.36b) along the interface:

$$\psi = \phi - \int_A^B \mathbf{H}_{st} \, dt \tag{2.37}$$

At the interface, the residuals for each region can be derived using (2.25) as:

$$R_1 = \int_{\Omega_1} \bigtriangledown \lambda_i \cdot \mu \bigtriangledown \psi \, d\Omega_1 - \int_\Gamma \lambda_i \, \mu \frac{\partial \psi}{\partial n} \, d\Gamma, \tag{2.38a}$$

$$R_2 = \int_{\Omega_2} \bigtriangledown \lambda_i \cdot \bigtriangledown \phi \, d\Omega_2 - \int_\Gamma \lambda_i \, \frac{\partial \phi}{\partial n} \, d\Gamma, \tag{2.38b}$$

where Γ is the boundary interface between two region. μ_2 has been taken out from (2.38b) as it is assumed constant in the region Ω_2. The sum of the residuals should be zero, i.e. $R_1 + R_2 = 0$. Then, considering the boundary condition requirements, (2.36a) and (2.37), continuity of the weight functions,

and the residuals condition, the contribution for an element with the nodal points on the interface is given in a matrix form as[46;47]:

$$F = Kg - h, \tag{2.39}$$

where K is the stiffness matrix (2.26), and g and h are column vectors defined as:

$$g = \int_A^B H_{st}\, dt, \tag{2.40a}$$

$$h = \int_\Gamma \lambda_i\, H_{sn}\, d\Gamma. \tag{2.40b}$$

In summary, the double scalar potentials ($\psi\phi$) approach can be applied to numerically solve the magnetostatic problem with the presence of material with high permeability by the use of (2.26). Then, (2.39) can be applied for the nodal points on the interface.

2.5 Optimization Strategies

Optimization methods are applied to solve problems in many different fields such as engineering, science, and economics. They are used for modeling, designing devices and circuits, solving system of equations, curve fitting, and much more. Problems solved using the optimization methods are formulated

mathematically with a function (f) as:

$$F = f(x_1, x_2, ..., x_n). \tag{2.41}$$

The function is called the objective function, F is a scalar quantity, and $x_1, x_2, ...,$ and x_n are variables. They are usually formulated in a matrix form, where variables form a vector called the design vector. The optimization algorithm is employed to find a design vector in such a way that minimizes (or maximizes) the objective function. The algorithm usually starts with an initial guess for the solution, then the solution is gradually improved by applying a numerical procedure iteratively until the final goal of optimization is achieved[48].

Optimization problems for real-life applications are complex, and they have a large number of variables, and there is no detailed prior knowledge of the shape and behavior of the objective function. They usually have multiple solutions: some of these solutions are the local optima, but the desired solution is the minimum (or maximum) of all the local optima (the global optimum). The process of assessing the entire solution space to find the global optimum is very expensive, meaning the optimization process will take too long. A hybrid combination of two optimization algorithms can be used to avoid this difficulty and increase the search efficiency. An algorithm with low cost can be used to do a search over the solution space to find the approximate location of the global optimum. Then, a second algorithm with low error can be applied to refine the approximate solution, which usually guarantees convergence to

the global optimum[49;50].

The optimization algorithms used in this work are the particle swarm optimization (PSO), for the global search, combined with a simplex method to fine tune the solution. The algorithms will be introduced and discussed briefly in the following sections.

2.5.1 Particle Swarm Optimization

PSO was originally introduced by Kennedy and Eberhart[51], inspired by the collective behavior and social characteristics of organic swarms such as flocks of birds or schools of fish. Therefore, it is a population-based algorithm looking for the global optimum.

A swarm of n particles is considered to start the optimization process; each particle represents a potential solution for the optimization problem. Two vectors are assigned to each particle to navigate through the space of candidate solutions: a position vector and a velocity vector. The position of each particle is the design vector with D components, where D is the number of the variables in the model. The algorithm starts with random positions and velocities within a defined range. Then, the velocity vector updates intelligently at each iteration, for each particle, and the position vectors are updated based on their velocities. The velocity (v) and position (x) vectors

of the i^{th} particle at the $k+1^{th}$ iteration are updated as follows:

$$v_i(k+1) = w\ v_i(k) + c_1\gamma_{1i}(P_i - x_i(k)) + c_2\gamma_{2i}(G - x_i(k)), \quad (2.42a)$$

$$x_i(k+1) = x_i(k) + v_i(k+1), \quad (2.42b)$$

where w is the inertia weight factor, c_1 and c_2 are the acceleration factors, and γ_{1i} and γ_{2i} are two independently random variables distributed between 0 and 1. The randomness of γ_{1i} and γ_{2i} contributes to the stochastic nature of the algorithm. In addition, each particle keeps track of the best solution observed by particle i, P_i (local best), and the best solution observed by the swarm, G (global best).

At each iteration, the position vector (2.42b) updates using three pieces of information, which correspond to three terms in (2.42a)[49;52]. The first term is the inertia term that controls how the particle can turn. The inertia weight (w) was set to be one for the original version of the PSO[51]. However, it has been shown that the algorithm performance can be improved if the variation of w (< 1) is considered[53;54;55]. The optimization starts with a large inertia weight, which means that the particle takes longer to turn, and therefore it searches a larger portion of the solution space. As the optimization progresses, w decreases. The second term is the cognitive term, which controls how the particle pursues it's own local best solution. Finally, the last term is the social term, which controls the movement of the particle toward the global best solution. Therefore, c_1 and c_2 determine the weights of the cognitive and social terms, respectively. Different considerations used to de-

termine these parameters for PSO algorithm are discussed in the literature[56].

The random nature of the control parameters in (2.42a) results in an explosion of the swarm, which means the velocity and position values reach to infinity in an uncontrolled way[54]. To avoid particle explosions, a limit is considered for each component of the velocity vector, and is defined as v_{max}. Thus, if the value of the velocity ($|v|$), calculated by (2.42a), exceeds v_{max}, it would be set to v_{max}[49].

The optimization algorithm defined above is a generic form of the PSO algorithm, and is used for this work. A 2D array of points are defined on the pole plate surface of the magnet. The component of the position vector for each particle is the thickness assigned to each point. Eight particles were chosen for the swarm. Then, parameters for (2.42a) were chosen based on Trelea type of PSO[55] where $c_1 = c_2 = 2$ and the inertia weight factor (w) starts with 0.9 and linearly decreases to 0.4. The maximum velocity was set to be 4.

The generic PSO suffers from premature convergence and it can easily get trapped in local optima. Combination of the PSO with other techniques, such as the genetic algorithm (GA), have been developed to prevent convergence toward local optima[57;58;59]. In addition, the PSO algorithm progresses fast initially, but it slows down. As mentioned before, a hybrid combination of algorithms can be applied to speed-up the process[49].

2.5.2 Pattern Search Algorithm: Nelder-Mead Simplex Method

The pattern search algorithm is a subset of direct search methods, which are used to minimize nonlinear unconstrained problems, defined by an objective function f. Using the direct search method, there is no need to calculate the derivative of f either exactly or approximately during the process. A key characteristic of the pattern search algorithm is that the search is performed by use of a pattern of points, where the pattern is independent of the objective function f[60].

The Nelder-Mead simplex method was introduced by Nelder and Mead in 1965[61]. The simplex-based algorithm is a multidirectional search that finds the minimum of a nonlinear function with n variables. An initial guess is required to start the process. Then, an initial simplex with $n + 1$ vertices is formed, where the initial guess is one vertex and small variations of the initial guess are used for the rest of vertices. The value of the objective function at each vertex is computed, and the vertex with the worst value (the one with the highest function value) is discarded and replaced by a new vertex to generate a new simplex. Based on the algorithm steps, each iteration requires one or more objective functions to be calculated using test points. The test points are generated using different operators, including: reflection, expansion, contraction (in and out), and shrinking[62]. Hence, a sequence of simplexes with different shapes are generated during the process.

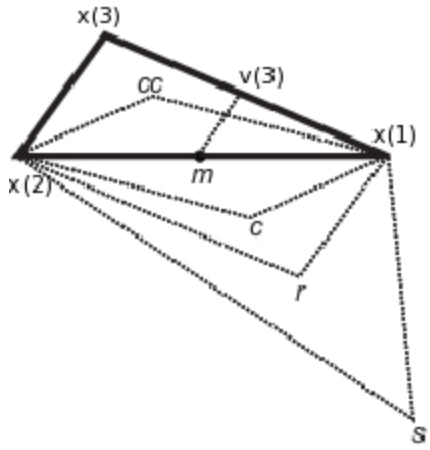

Figure 2.5: Triangles are formed when a function with two variables is minimized: the triangle with bold lines is the initial simplex, and the triangles with dashed lines are formed at different steps of the minimization process based on which operators are acting on the initial triangle.

In the case of minimizing a function with two variables, a triangle is formed as the simplex. Figure (2.5) shows triangles formed during the optimization process. The triangle with bold sides is the initial triangle, and $x(3)$ is the vertex with the highest function value. The reflection operator generates the new point r in the direction away from the worst vertex, where the size and shape of the triangle is the same as the initial one. The expansion and contraction (in and out) operators generate points s, cc, and c respectively, where the size and shape of the original triangle is changed after applying each operator. The shrinking operator uses two points, $v(3)$ and m, to form a shrunk triangle[(52)]. Both points are moving toward the best vertex ($x(2)$), which has the lowest function value. The iteration terminates by forming a new simplex, which has vertices with function values that meet a descent condition compared to the previous simplex[(63)]. With a proper initial guess,

the pattern search algorithm converges quickly to the local optimum.

The simplicity of the algorithm makes it a popular optimization technique for computational implementation, and it is a standard optimization method available in MATLAB using $fminsearch$ command[64].

For this work, the PSO algorithm is used to search the solution space for a global minimum. The convergence rate slows down as the algorithm proceeds. At this stage, the final solution for the PSO algorithm is used as the initial solution for the Nelder-Mead simplex method. This method applies to fine tune the solution.

Chapter 3

Preliminary Design Evaluation

The basic design concept of the envisioned model consists of a steel biplanar yoke with superconducting coils around the supports, and steel projections attached to the pole plate to guide magnetic flux toward the region-of-interest. The exact nature of the steel projections that would best serve our needs had yet to be determined. Additionally, optimization schemes needed to be evaluated for their effectiveness. To accomplish these goals, a closed symmetrical model (model with no patient access) with different structures for projections was studied due to its simplicity. In addition, the symmetrical model is faster to simulate, allowing a more rapid response for these preliminary investigations.

Various design concepts were explored to identify the one with optimal characteristics. Finite-element analysis was used to test and optimize the magnet designs using the 3-D FEM software package Opera-3D[30]. In addition, the optimization algorithm, used in MATLAB[64] to guide the convergence to a

solution, needed to be investigated to ensure a fast and robust solution that avoids local minima.

Two different structures for projections were investigated for the symmetrical magnet assembly: the tapered conical projections and the continuous cylindrical projections. The tapered conical projections model was used initially as it was assumed that the tapered conical projections can provide a means to direct the magnetic flux and it had limited number of variables to be optimized. However, it became impractical due to the insufficient space. More projections were needed to improve the homogeneity but they started to overlap. To get around the overlap problem, the continuous cylindrical projections model were investigated where there was no restriction since the projections were adjacent.

Finding the appropriate optimization algorithm and the optimal pole plate structure for the closed symmetrical model lead us to the next step, which is the optimization of the pole plate surface for an open access non-axial model.

3.1 Evaluation of a Tapered Projection Approach

A tapered conical design is shown in figure (3.1). The projections for the tapered conical design are added to the pole plate as tapered conical projections. The material used for both yoke and pole plate assembly in the closed

symmetrical model is SiSteel. Using materials with high magnetic susceptibility confines the magnetic flux inside the magnet, and this provides a path through which the magnetic flux is manipulated to pass through the projections. For this model, there are two superconducting loops with currents in opposite directions in the vicinity of the yoke to generate a maximal flux in the material of the yoke supports.

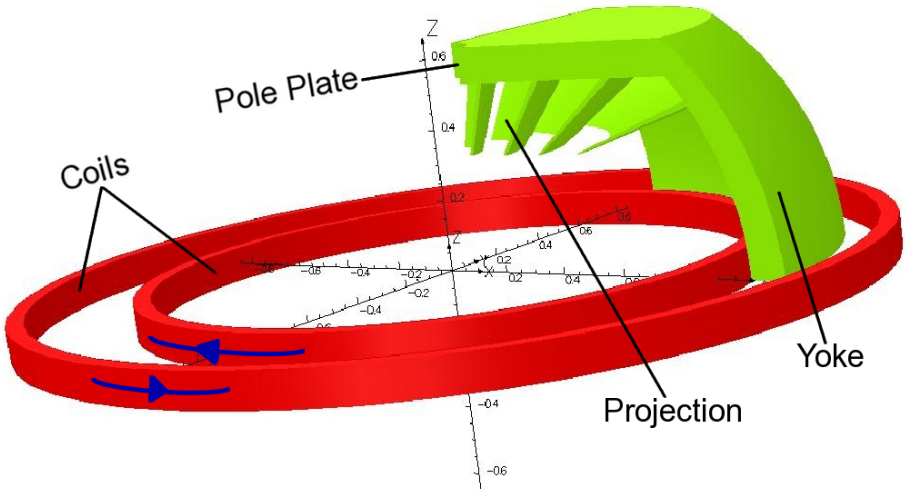

Figure 3.1: One-eighth of the tapered conical projections model. Blue arrows show the direction of currents.

In a tapered conical design, the projections can be oriented at a specific angle to direct the magnetic flux toward the region of interest inside the field-of-view, which is an ellipsoid with its centre located at the isocentre. Before the optimization, the field is non-uniform inside the imaging field-of-view. However, the location and orientation of each projection can be optimized to manipulate the magnetic flux inside the field-of-view and alter the magnetic field to a uniform one. Since the permeability of the steel is so much higher

than that of the air gaps in between, it was hoped that the bulk of the available magnetic flux at the pole plate would be directed along the length of the projections, providing a means to direct the field.

For this design, the optimization methods were applied to find the optimum number of projections, the orientation, and the location of each projection.

3.1.1 Independent Projections Approach

Considering that the field lines would follow the same direction as the direction of a projection after leaving it, the projections were first assumed to act independently for an independent projections approach. Hence, the problem can be defined as a linear one, where:

$$B = \sum_{i=1}^{n} B_i. \tag{3.1}$$

B is the magnetic flux at a point inside the magnet for a model with n projections. B_i is the magnetic flux at the same point resulting from a model with a single projection, where this projection has already been defined in the model with n projections. By these assumptions, the linear model defined as $B \times \mathrm{x} = 0.5 \times \mathrm{I}$ is solved for $\mathbf{x}$. In detail, one has:

$$\left(\begin{array}{c|c|c|c} \overset{\alpha_1, r_1, t_1}{\vphantom{x}} & \overset{\alpha_2, r_2, t_2}{\vphantom{x}} & & \overset{\alpha_{n_P}, r_{n_P}, t_{n_P}}{\vphantom{x}} \\ B_{1,1} & B_{1,2} & \cdots & B_{1,n_P} \\ B_{2,1} & B_{2,2} & \cdots & B_{2,n_P} \\ \vdots & \vdots & \ddots & \vdots \\ B_{n_t,1} & B_{n_t,2} & \cdots & B_{n_t,n_P} \end{array}\right)_{n_t \times n_p} \times \begin{pmatrix} x_1 \\ x_2 \\ \vdots \\ x_{n_p} \end{pmatrix}_{n_p \times 1} \cong 0.5 \times \begin{pmatrix} 1 \\ 1 \\ \vdots \\ 1 \end{pmatrix}_{n_t \times 1} . \tag{3.2}$$

Each column of matrix **B** has the magnetic flux values for a model of an individual projection with a defined orientation presented by angle α_p, location presented by radius r_p, and thickness t_p. n_p is the number of different scenarios and n_t is the number of targets points. A target surface is defined as an ellipse with large axis (Y) of 0.60 m and small axis (Z) of 0.40 m. Magnetic flux is calculated at 400 points for one-eighth of the ellipse. The matrix **x** is a binary matrix and 0.5 T is the desired magnetic flux at the isocentre.

Matrix $(B)_{400\times5}$ considers five independent projections and the matrix $(B)_{400\times1}$ uses all five projections together in a model were calculated to check the linearity assumption. In general it was found that equation (3.3) is substantially inaccurate, indicating that this projection model could not be approximated as a linear system.

$$(B)_{400\times5} \times (\mathrm{I})_{5\times1} \neq (B)_{400\times1} \,. \tag{3.3}$$

3.1.2 Pole Plate Optimization

After the linear system was shown to be insufficient, a nonlinear optimization approach was attempted to define the optimal position and angle of each projection with all projections included in the model. A cost function is defined as:

$$f = \int_A [B(\overrightarrow{\mathbf{r}}, \overrightarrow{\mathbf{P}}) - B_o]^2 \ da. \tag{3.4}$$

A is a target surface, the field-of-view, defined as a 2-D ellipse with a large axis (Y) of 0.60 m, a small axis (Z) of 0.40 m, and its center located at the isocenter. Due to the symmetry, magnetic flux was calculated over 400 uniformly distributed points for one-eighth of the ellipse. $B(\overrightarrow{\mathbf{r}}, \overrightarrow{\mathbf{P}})$ is the magnetic flux at point $\overrightarrow{\mathbf{r}}$ on the target patch for $\overrightarrow{\mathbf{P}}$. $\overrightarrow{\mathbf{P}}(r_2, ..., r_n, \alpha_1, ..., \alpha_n)$ is the design vector including all variables in the design. r_n is the radius of the n^{th} tapered cone at the XY plane for Z equal to 0.33 m. r_1 is constant and equal to 12 cm to accommodate the 24 cm diameter hole at the center of the magnet assembly that allows for the passage of radiation. α_n is the projection's polar angle at Z equal to 0.33 m.

Two optimization algorithms were used to find the minimum of the cost function. The gradient descent algorithm searches for the minimum in the gradient direction. The algorithm converges to the local best solution. The initial guess of the solution is important to guide us toward the minimum value. This algorithm was used at early stage of the optimization. However, the gradient should be calculated at each iteration so it is not the best choice

for this model when the number of projection increases. The Nelder-Mead simplex method is applied to find the minimum of a nonlinear function of n real variables without using any derivative information[63].

It is important to have a good initial guess for both algorithms. The solution for a 0.5 T homogeneous magnetic field over an ellipse, which is similar to the elliptical target field, with a large axis (Y) of 0.60 m and a small axis (Z) of 0.225 m, was used to find a reasonable initial guess to start with. The vector map of this solution was used to find the direction of the magnetic field at $Z = 0.33$ m, shown in figure (3.2).

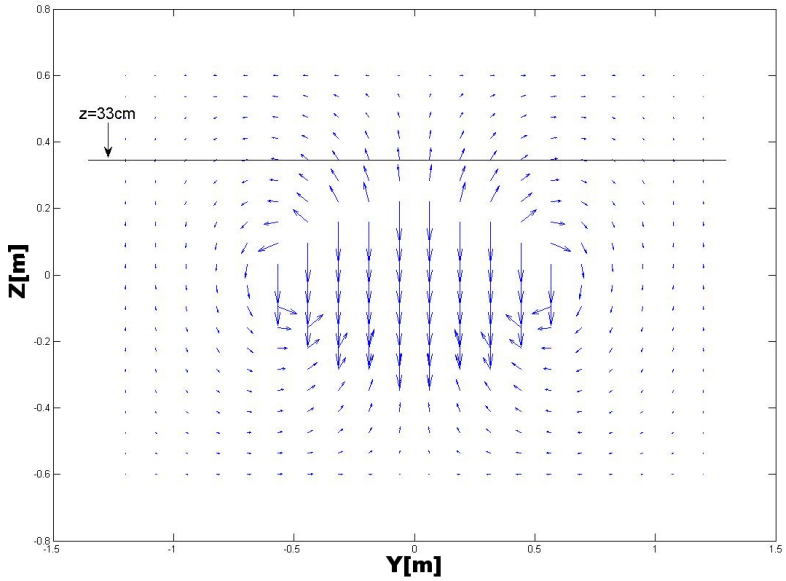

Figure 3.2: Vector map for a 0.5 T homogeneous magnetic field solution.

A quantity called $Fill\_Density$ is defined as $\frac{B_{norm}(y)}{B_{sat}}$. B_{norm} is the magnitude of the magnetic flux at Z equal to 0.33 m and B_{sat} is the saturation field

for SiSteel, which is 1.95 T. The first projection starts at Y equal to 0.12 m because there is a hole with a 0.24 m longitudinal diameter at the center of the magnet assembly. This hole is intended to be used as a path for radiation to pass through the yoke in the final design. The thickness of each projection (T) is assumed to be 1 cm. The gap (G) between each projection is calculated by the following equation:

$$\frac{T}{Gap} = \frac{Fill\_Density(Y)}{1 - (Fill\_Density(Y))}. \tag{3.5}$$

Four positions were found to locate each projection with the angles specific to $Y \in$ [0.12 m, 0.60 m], illustrated in figure (3.3). The angle is defined as $arctan(\frac{B_z(Y)}{B_y(Y)})$.

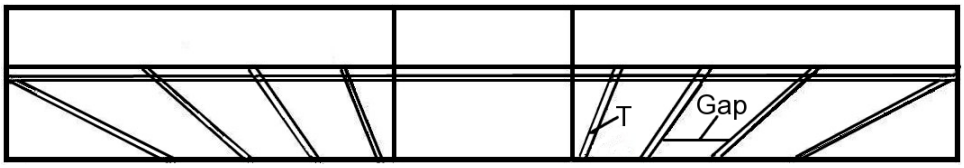

Figure 3.3: Cross-sectional view of the pole plate with projections.

More projections were added to the pole plate based on the study of the elliptical map of the magnetic flux at the center. The results are reported in table (3.1).

The advantage of this design was its ability to steer the magnetic flux by manipulating the angle of the conical projections. Despite this advantage, the results showed that obtaining good uniformity is difficult using this model.

Structure		Optimization		
no. of Projections	no. of Variables	Algorithm	fval_i	fval_f
4	7	Steepest Descent	2.13×10^{-3}	5.29×10^{-4}
5	11	Steepest Descent	5.96×10^{-4}	4.69×10^{-4}
		Simplex Method	4.69×10^{-4}	4.06×10^{-4}
7	13	Simplex Method	1.27×10^{-3}	3.89×10^{-4}

Table 3.1: Results of the tapered conical projections model. The $fval$ is the value of the cost function, f, defined by (3.4). Two variables are assigned to each projection: the radius and the polar angle of the projection. however, the radius of the first projection is fixed at 0.12 m. Therefore, the number of variables are $2n-1$ for n projections model.

Therefore, a model with continuous cylindrical projections was investigated.

3.2 Determination of Optimization Algorithm Using Continuous Projections

The continuous projections design consisted of $n = 15$ contiguous cylindrical structures located at the pole plate from raduis of 0.12 m to 0.87 m with 5 cm thickness, showed in figure (3.4). The cost function is defined by (3.4) with the same target surface. The design vector $\overrightarrow{\mathbf{P}}(l_1, ..., l_{15})$ includes the variables, which are the lengths of each projection. The length should be within the range of 0.35 - 0.60 m.

Using the gradient descent algorithm is likely a poor choice for this design because we have 16 parameters to optimize and the minimization would be a time-consuming process as the gradient of the objective function should be calculated at each iteration. The simplex method and the particle swarm

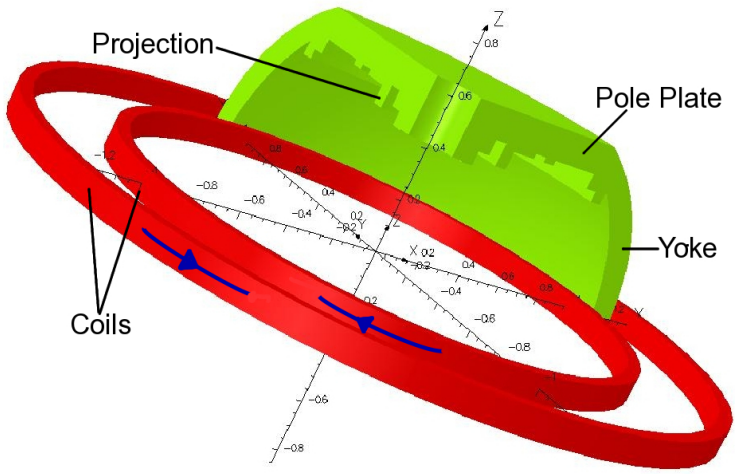

Figure 3.4: One-eighth of the continuous projections model. Blue arrows show the direction of currents.

optimization (PSO) algorithms were investigated for this design. The PSO is a stochastic, population-based algorithm modelled on the social behaviour of a flock of birds or a school of fish[57]. It is a derivative-free search for a global best solution.

Structure	Optimization		
no. of Projections	Algorithm	fval_i	fval_f
15	PSO	3.40×10^{-3}	2.93×10^{-5}
	Simplex Method	2.93×10^{-5}	2.52×10^{-5}

Table 3.2: Results of the continuous cylindrical projections model

The results of optimization are reported in table (3.2). Based on the two orders of magnitude of improvement in homogeneity using the PSO, this algorithm was found to converge in an acceptable way for this design. In addition, the simplex method can be used for fine tuning of the solution.

The preliminary evaluations of the design lead to use the continuous struc-

ture for the pole plate assembly in the final non-axial model, where the pole plate surface is divided into n cylinders and the thickness of the pole plate is optimized based on the consideration that the design is a non-symmetric model.

Chapter 4

Open-Access Non-Axial Model

A version of this chapter has been submitted for publication. S. Yaghoobpour Tari, K. Wachowicz, and B. G. Fallone, "A Non-Axial Superconducting Magnet Design for Optimized Patient Access and Minimal SAD for Use in a Linac-MR Hybrid: Proof of Concept", (2016).

Preliminary design evaluation equipped us to work on the final non-axial magnet design. The final magnet assembly has similar components to the continuous cylindrical projections model except an opening for the patient. A rectangular section of the yoke for the closed model is cut out to create an opening for the patient access, as shown in figure (4.1). Two superconducting loops with currents in opposite directions used in (3.1) and (3.4) simulate the similar situation as the open-access non-axial system however this opening clearly prevents a continuous coil from surrounding magnet as in the preliminary designs. Further, it was found that if the same coil design was modified to wrap around each yoke support, only a field of approximately 0.2 T could

be created. Hence, the distribution of coils should be modified to generate a 0.5 T magnetic field at isocentre, which is the field of interest for the Linac-MR system. Finally, finite-element analysis and optimization algorithms were applied to find the optimum surface of the pole plate, which yields the desired uniformity over a field-of-view suitable for MR imaging.

The detailed characteristics of the non-axial magnet assmbly, pole plate optimization method, and results for both magnet designs with 0.2 T and 0.5 T are described in the following sections.

4.1 Magnet Assembly

The open superconducting magnet assembly is depicted in figure (4.1). The superconducting coils have been moved from their conventional position (being centred on the magnet axis, with one adjacent to each pole plate) to a non-axial position surrounding the yoke supports. The yoke supports are composed of American Iron and Steel Institute (AISI) 1020 plain carbon steel and serve both a mechanical and magnetic function, the structure may need to be further fortified with non-magnetic supports. Mechanically they resist the compressive force between the two magnetic poles, and magnetically they serves as a flux pathway, guiding magnetic flux generated by the coils to the pole plates, which are sculpted to distribute the field uniformly over a region-of-interest. The pole plates are composed of grain-oriented (GO) silicon steel. A grain is small crystal that forms inside the solid metal. GO silicon steel is developed under controlled condition to produce grains with preferred crystal

orientation, known as Goss texture[65], which improves magnetic properties in the rolling direction. The GO silicon steel is a high-permeability material, and can be constructed out of laminated sheets to resist the formation of eddy currents during MR imaging. Eddy currents are induced in metals by rapidly changing fields of RF and gradient coils due to the Faraday's law[45].

The sculpted nature of the pole plates, as described above, is achieved by considering this structure to be defined by a continuous array of vertical projections, each of which guides magnetic flux toward the target region, an ellipsoid with its center located at isocentre. In this work, a homogeneous field over the target region is achieved by optimizing the height of all these projections. This procedure will be described in more detail below.

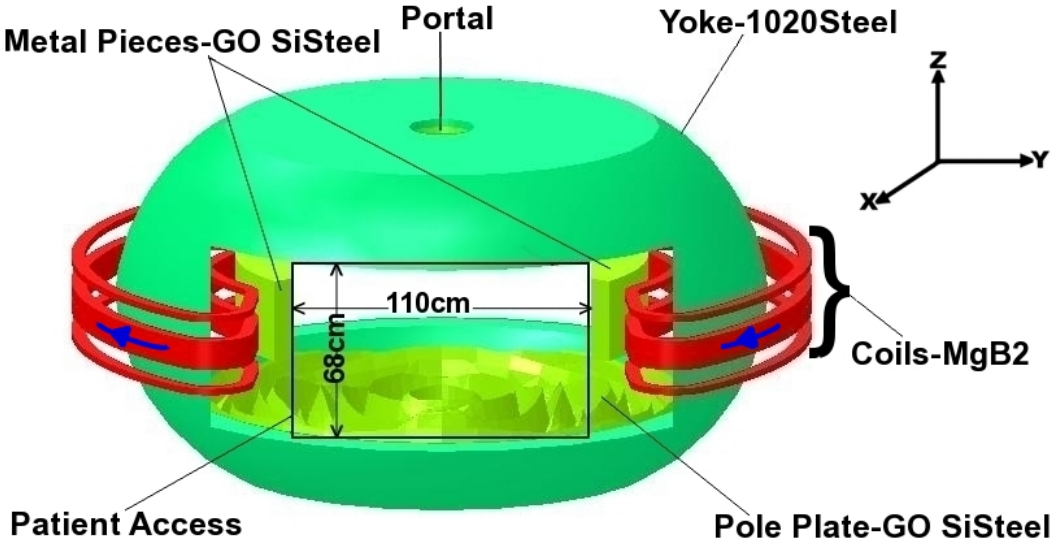

Figure 4.1: 3-D schematic of the magnet assembly.

In this proof of principle design, the minimum gap between two pole plates is

set to 68 cm and the distance from the isocentre to the yoke's top is 63 cm, which results in a SAD equal to 123 cm. This assumes a 60 cm distance between the target and the top of the yoke, which is distance from target to end of the MLC for the standard, unmodified Varian 600C linac head (Varian Linac Document; Drawing number: 1106021). There is an opening with a diameter of 24 cm bored through the magnet to open a path for the radiation. The linac head would be placed on the top of the outer surface of the magnet into which the portal is drilled, and it is the height of this surface relative to isocentre that would ideally be minimized. Further, this yoke design is constructed to maintain the 110 cm lateral patient access that the current model allows, being important for patient comfort and treatment flexibility.

4.1.1 Distribution of Coils

In this design, the material used for the superconducting coils is MgB_2, which is a high-temperature superconducting (HTS) material[39]. This superconductor ($T_c \sim 39$ ^{o}K) allows for greater flexibility, especially for a rotating magnet, as no cryogens need to be stored at the coils, given that the coils can be conduction cooled[40]. In this work, the current density for the MgB_2 coil is assumed to be 2.1×10^8 Am^{-2}, as was done in previous work on magnet design for linac-mr[66]. This current density is theoretically achievable at temperature of 10 ^{o}K and a magnetic field of 6.5 T[67], even assuming a superconducting fill factor of only 20%. However, any implementation will be very dependent on the exact manufacturing process of the wire, and therefore the exact conductor distribution will need to be considered on a case-by-case

basis, given that each conductor yields different specifications in terms of critical field, temperature and current density.

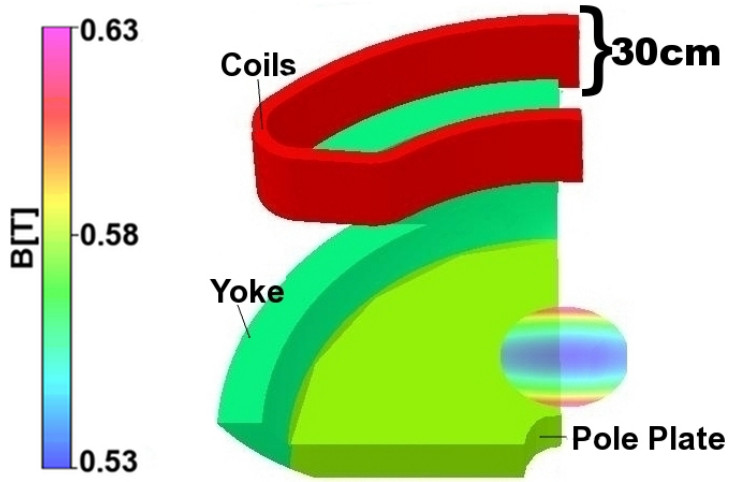

(a)

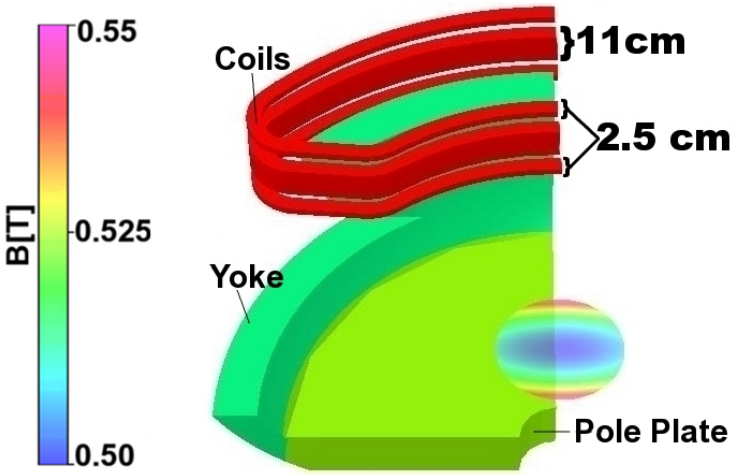

(b)

Figure 4.2: (a) One-eighth of the magnet with a thick coil, (b) one-eighth of the magnet with three distributed coils.

For this proof-of-principle implementation, different scenarios were explored to find a suitable current distribution. Two examples of these distributions

are shown in figure (4.2). These examples reveal the non-linear nature of the current distribution with respect to the field produced at isocentre. The magnetic field generated at the isocentre is about 0.5 T for a solid coil with thickness of 30 cm, illustrated in figure (4.2a). On the other hand, a 0.5 T magnetic field can be generated by a coil distribution where the thickness of the middle coil is 11 cm and the thickness of two outer coils is 2.5 cm, illustrated in figure (4.2b). The gap between the top and bottom coils is 25 cm. Therefore, roughly the same field with considerably less current cross section can be produced using distributed coil elements. This can be explained by the fact that the AISI 1020 steel yoke supports saturate magnetically above roughly 2T, after which additional current surrounding a similar location will provide little additional flux through isocentre.

Magnetization of the magnet, M, measures the magnetic response of the magnet and is calculated by:

$$M = \frac{B}{\mu_0} - H. \tag{4.1}$$

Figure (4.2) illustrates magnetization of the yoke support for aforementioned coil configurations. Both distributions generate the same level of magnetization, which means that they are fully saturated.

This coil distribution was not optimized exhaustively, and there may well be more efficient designs. However, given that our primary interest was the ability to sculpt a homogeneous field in this non-axial design by manipulation

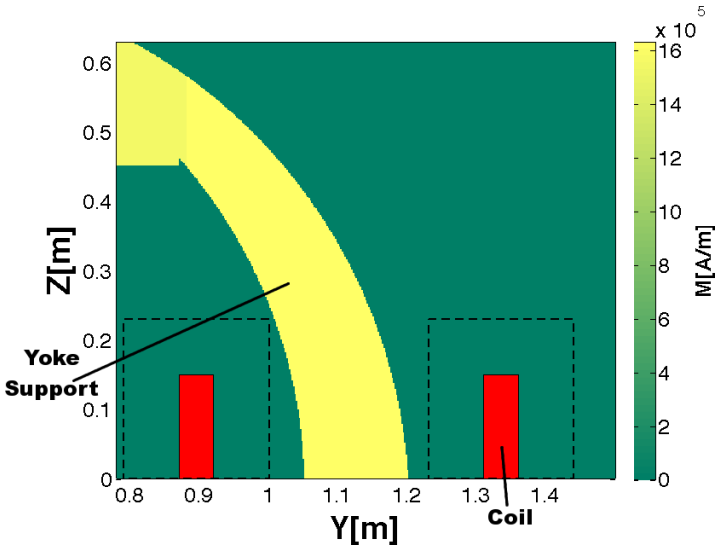

(a)

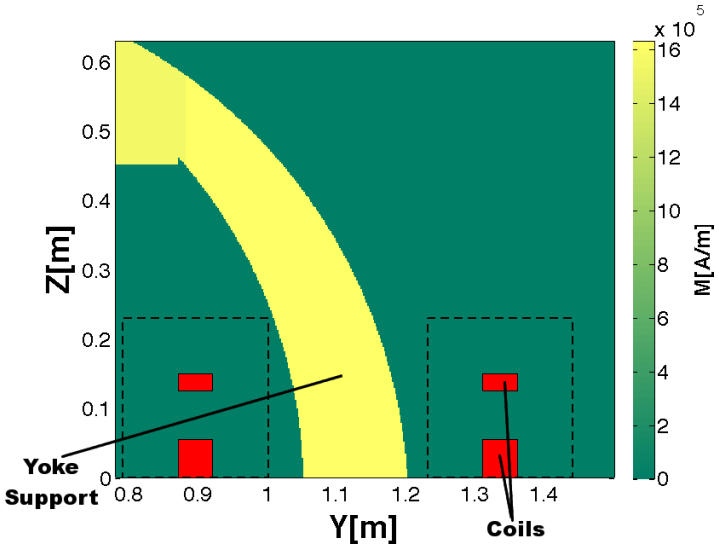

(b)

Figure 4.3: Cross-section of the magnet in YZ plane. In addition, cross sections of the cryostat are shown in dashed lines. The cryostat is extended 8 cm beyond the coil at each side. (a) Magnetization of the yoke support for a thick-coil configuration, (b) Magnetization of the yoke support for a three-coils configuration. Although the total current is different between the panels, the magnetization is essentially identical due to the materials being magnetically saturated.

of the pole plates, the three-coil distribution as shown in figure (4.2b) was used for the 0.5 T design.

Considering the points distributed over a circular surface around the isocenter, the points in the regions close to the superconducting coils create hot spots, such as the magnetic field map shown in figure (4.2). This makes the optimization process difficult and this problem cannot be addressed by the pole plate optimization alone, since there is not enough room with the pole plate for the adjustment to accommodate these hot spots. Therefore, two bulk metal shims consisting of GO silicon steel were added in the vicinity of the coils to compensate. The presence of these bulk metal shims pulls some of the excess magnetic flux away from the field of interest and partially corrects for the hot spots seen on the lateral edges.

4.2 Method

4.2.1 Magnetic Field Simulation

The magnetic field calculations in this work were performed with the 3-D FEM software package Opera-3D[30], using a magnetostatic model. The electromagnetic analysis is based on the following Maxwell's equations:

$$\bigtriangledown \times \mathbf{H} = \mathbf{J}, \tag{4.2}$$

$$\bigtriangledown \cdot \mathbf{B} = 0, \tag{4.3}$$

where $\mathbf{H}$ is the magnetic field, $\mathbf{B}$ is the magnetic flux density, and $\mathbf{J}$ is the current density.

The total magnetic field $\mathbf{H}$ can be defined as[46;47]:

$$\mathbf{H} = \mathbf{H}_c + \mathbf{H}_m. \tag{4.4}$$

$\mathbf{H}_c$ is the magnetic field from the conductor, which can be calculated using the Biot−Savart law:

$$\mathbf{H}_c = \frac{1}{4\pi} \int_V \frac{\mathbf{J} \times \mathbf{r}}{|\mathbf{r}|^3} \, dV. \tag{4.5}$$

$\mathbf{H}_m$ is the rest of the field where $\bigtriangledown \times \mathbf{H}_m = 0$. Therefore, the magnetic field $\mathbf{H}_m$ can be determined by:

$$\mathbf{H}_m = - \bigtriangledown \phi, \tag{4.6}$$

where ϕ is the magnetic scalar potential.

Using the magnetic permeability, μ, the magnetic field and the magnetic flux density can be related by the following equation:

$$\mathbf{B} = \mu \mathbf{H}. \tag{4.7}$$

Given that the divergence of the flux density is always zero, the magnetic field can be derived using the following equation:

$$\bigtriangledown \cdot \mu \bigtriangledown \phi - \bigtriangledown \cdot \mu \left(\frac{1}{4\pi} \int_V \frac{\mathbf{J} \times \mathbf{r}}{|\mathbf{r}|^3} \, dV \right) = 0. \tag{4.8}$$

When there is a structure made of a material with high permeability in the problem, the difference between the first and second terms of (4.8) is quite small inside the high permeability region. Therefore, the error in the field calculation dominates the difference between the first and second terms of (4.8). To avoid this problem, the volume of the problem is divided into two regions[46;47]. The first region contains all the conductors and no material with high μ, where (4.8) is applied to calculate the scalar potential. The second region contains the material with the high permeability and no currents. Since $\mathbf{J} = 0$ in the second region, the scalar potential (ψ) is calculated for this region using $\bigtriangledown \cdot \mu \bigtriangledown \psi = 0$, which is derived from (4.2) and (4.3). Then the solutions for two regions must be matched at the interface of two regions with proper boundary conditions that are valid at the interface[46;47].

The nonlinear magnetization curves for the materials used in magnet are shown in figure (4.4). The AISI 1020 steel data are assembled based on data from[68;69] and the GO silicon steel are obtained from product documentation from AK steel (M-2MILL-ANNEAL grain-oriented electrical steel).

A large cube with a dimension of 12 m is set to be the outer boundary. The tangential magnetic field condition, $\mathbf{H} \cdot \mathbf{n} = 0$, was applied for the outer boundary, which is equivalent to $\frac{\partial \psi}{\partial \mathbf{n}} = 0$. $\mathbf{n}$ is the outward normal unit vector at the surface of the cube. However, the model is symmetric so one can solve only one-eighth of the model using three cutting planes, which are the internal boundary of one-eighth of the model. The internal XZ and YZ planes should have the tangential magnetic field condition. But, for the internal XY

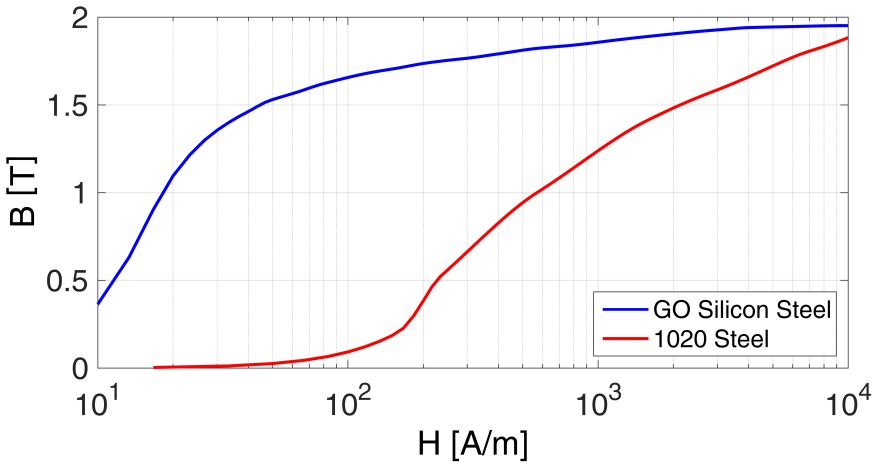

Figure 4.4: Magnetization curves for GO Silicon Steel and AISI 1020 Steel.

plane, the normal magnetic field condition was applied, $\mathbf{H} \times \mathbf{n} = 0$, which means having a constant scalar potential across this boundary plane. Given a well-defined boundary-value problem, the FEM technique can be applied to derive the scalar potentials ϕ and ψ numerically using Opera-3D, allowing for a magnetic field solution.

The FEM model is divided into approximately 1.3×10^5 tetrahedral elements. The sizes of the elements vary for the various compartments of the model. The minimum element size is about 1.5 cm for the surface of the target ellipsoid and the maximum size is about 240 cm for the outmost boundary. All elements are linear for all geometrical compartments of the model except the target ellipsoid where the quadratic elements are used to increase the accuracy.

4.2.2 Pole Plate Optimization

The outer surface of the pole plate is optimized subject to the minimization of a cost function, which evaluates the uniformity of the magnetic field over an ellipsoid. The cost function, f, is calculated as:

$$f = \int_A \ [B(\overrightarrow{\mathbf{r}}, \overrightarrow{\mathbf{P}}) - B_o]^2 \ \ da. \tag{4.9}$$

The cost function is the same function defined in the previous chapter. A is a target surface defined in this work as the surface of an ellipsoid with a major axis (Y) of 0.60 m, minor axes (X, Z) of 0.40 m, and its center located at the isocenter. Due to the symmetry, magnetic flux is calculated over only one-eighth of the ellipsoid surface, at 692 uniformly distributed points. The points are chosen to be equally distanced over the ellipsoid's surface. $B(\overrightarrow{\mathbf{r}}, \overrightarrow{\mathbf{P}})$ is the magnetic flux magnitude at point $\overrightarrow{\mathbf{r}}$ on the surface patch for $\overrightarrow{\mathbf{P}}$. $\overrightarrow{\mathbf{P}}(Z_1, Z_2, ..., Z_{N_r})$ is the design vector including variables, Z_i, in the design, where Z_i is the thickness of the pole plate for the defined point on the surface of the pole plate in the XY plane . B_o is the magnetic flux at the isocenter.

Considering the symmetry of the pole plate, only one fourth of the surface needs to be optimized. The pole plate quadrant is divided into four sections using five spokes, $N_{spk} = 5$, located at 0, $\pi/8$, $\pi/4$, $3\pi/8$, and $\pi/2$. Further, each spoke is represented by N_r control points as is displayed in figure (4.5). The inner radius of the pole plate is located at $r = 0.12$ m and its outer ra-

dius extends to $r = 0.87$ m. $N_r = 16$ and $N_r = 31$ evenly-spaced parameters were chosen in the radial direction for the 0.2 T design and 0.5 T design, respectively. Therefore, the distances between two control points is 5 cm and 2.5 cm for each case, respectively. This sampling density resulted in many optimization parameters, but given the unknown nature of the solution, it was felt that it was better to err on the side of excess samples than to impose a potentially limiting assumption to the sampling density.

The total number of control points on the surface of the pole plate in the XY plane are $N_{spk} \times N_r$. A value of Z_i is assigned to each control point. Using four neighboring points located in two adjacent spokes and arcs, a structure called a projection was constructed, as depicted in figure (4.5). The surface of the pole plate is constructed piecewise using these projections. In order to have a surface that remains faithful to the thickness at the four neighbouring points, defining the boundaries of the projection, the projection is divided into four triangular prisms. The middle point for the surface of the projection in the XY plane is the centre of the trapezoid, which is formed using four neighboring points, and the Z value of the middle point is the average Z values of those points.

The expectation of a smoothly varying pole plate in the azimuthal direction allows to model the variation of these control points as a Fourier series. The thickness (Z) for each point is defined as

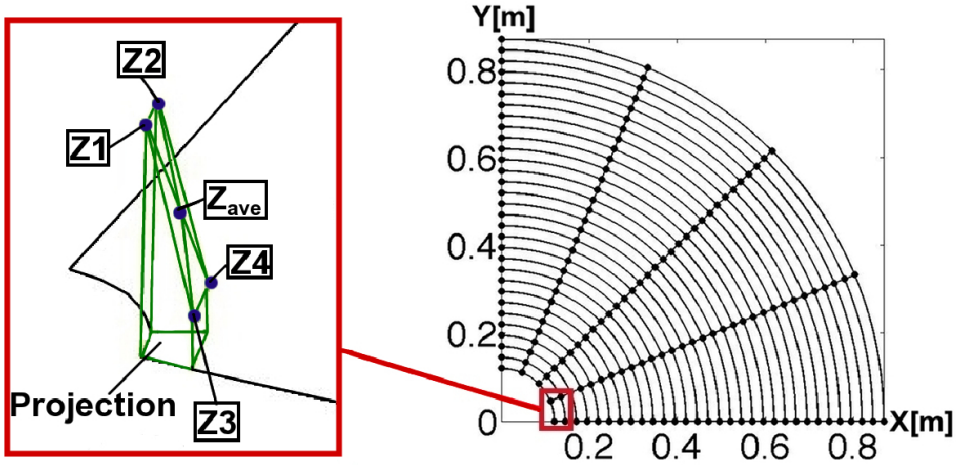

Figure 4.5: Points on the pole plate surface in the XY plane associated with the optimization variables Z_i. Z_{ave} is equal to the average values of the Z_i from the four neighboring points.

$$Z = \sum_{n=0}^{N} C_n(r_k) e^{-in\theta_j}, \tag{4.10}$$

where r_k is the radial coordinate of point k on $y = 0$ axis and θ_j is the angle of each spoke. The pole plate surface faced toward iso-centre is shown in figure (4.6); the parts with the same color should have the same structure.

The model is symmetric about $\theta = 0$. Therefore, by removing the anti-symmetric terms of (4.10), one has:

$$Z = \sum_{n=0}^{N} A_n(r_k) cos(n\theta_j). \tag{4.11}$$

Given that by design the model must be periodic in π, only even frequencies are permitted. Therefore if the series is truncated at $N = 4$, the pole plate's

thickness can be modeled as

$$Z = A_0(r_k) + A_2(r_k)cos(2\theta_j) + A_4(r_k)cos(4\theta_j). \tag{4.12}$$

Therefore, the thickness of the pole plate can be defined by equation (4.12) using low-resolution sinusoids with even coefficients of θ_j. Using (4.12), the total number of parameters are reduced from $N_{spk} \times N_r$ to $3N_r$ since the points on one arc but different spokes are not independent.

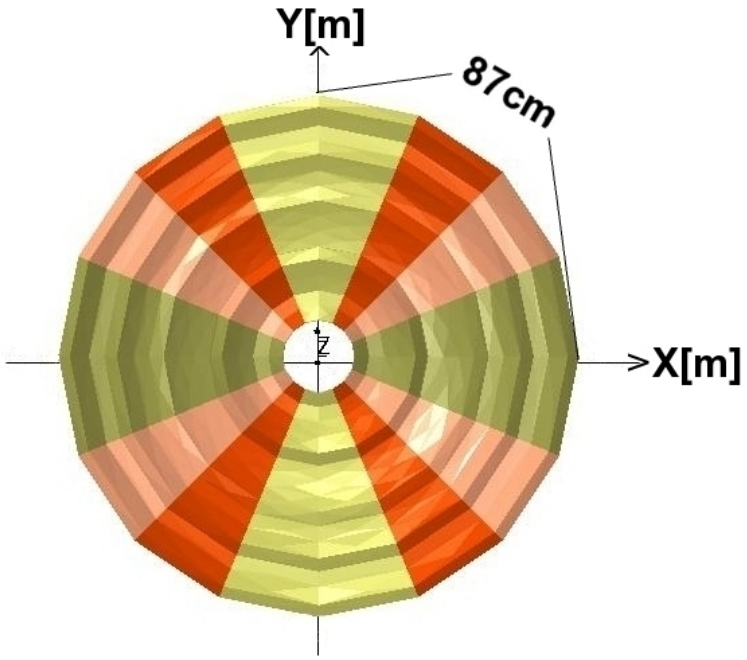

Figure 4.6: The surface of the pole plate in the XY plane.

The surface of the pole plate is optimized in 3 steps by considering one term of equation (4.12) at each step. $A_0(r_k)$, $A_2(r_k)$, and $A_4(r_k)$ are the variables at each step. This further reduces the number of parameters at each stage of the

optimization to N_r. The optimization was started with five spokes in angular direction. For 0.5 T design, after all three terms in (4.12) were optimized, the resolution was increased in the angular direction to nine spokes using the best result for five spokes to avoid the sharp edges in azimuthal direction.

Because of having many variables to be optimized, the particle swarm optimization (PSO)[57], which is a stochastic algorithm searching for the global best solution, was found to be the most suitable choice to do the optimization. The pattern search algorithm, on the other hand (also known as the Nelder-Mead simplex method[63]), can be used as a complementary algorithm to locate the local best solution after the PSO search for the global minimum. The simplex method is a derivative-free algorithm that converges quickly to a local minimum and it requires a good initial solution. Therefore, as mentioned before, the PSO was used as the prime algorithm for the optimization and the simplex method was used for the fine-tuning of the solution.

During the optimization of the 0.5 T design, the PSO optimization scheme was at times found to be mired in a local minimum, as is known to be an issue with optimization schemes of this type[59]. Given sufficient iterations, the optimization may have escaped the minima, but given the lengthy iteration times ($\sim$ 90 minutes for all particles in 0.5 T case), the operator occasionally found the need to intervene. At such a time, a manual solution (constructed by the operator) was introduced to prompt the algorithm to escape the local minimum and return to its optimization.

4.3 Results

4.3.1 0.2 T Model Results

For the 0.2 T model, a single coil is located at each side of the yoke, shown in figure (4.7). The thickness of the coil is 10 cm. The optimization was started by assigning Z_i to 0.45 m at all control points on the pole plate. The value for the objective function, f_{val_i}, defined by (4.9) was 3.93×10^{-2}. The optimization was started without bulk metal shims to investigate the possibility of hot spot accommodation just by pole plate optimization. When the necessity of the bulk metal shim's presence was realized, the optimization was started with the addition of the bulk metal shims. The effect of adding a bulk metal shim is illustrated in figure (4.9). To speed up the optimization process, the solution from the optimization without the bulk metal shims was used as the initial solution for the optimization with the bulk metal shims. The results from the minimization of the objective function are shown in table (4.1).

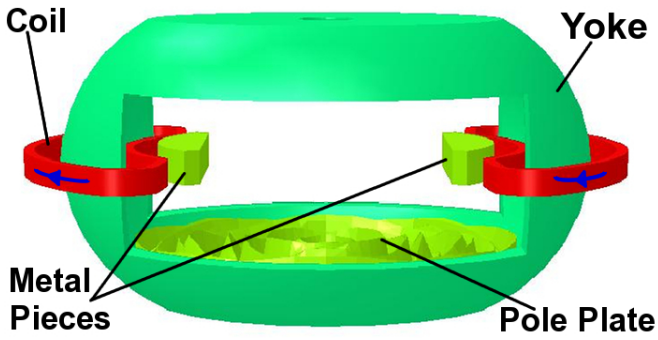

Figure 4.7: 3-D schematic of the magnet assembly for 0.2 T design.

Structure	Optimization		
Projections	Algorithm	fval_i	fval_f
16 Projections	PSO-First Term	6.31×10^{-4}	1.79×10^{-5}
	PSO-Second Term	1.79×10^{-5}	1.64×10^{-5}
	PSO-Third Term	1.64×10^{-5}	9.61×10^{-6}

Table 4.1: Optimization results for the 0.2 T model

The inhomogeneity of the field over the defined surfaces for the final solution is measured using:

$$\Delta B = max\left(\left|\frac{B(\overrightarrow{\mathbf{r}}) - B_o}{B_o} \times 10^6\right|\right), \tag{4.13}$$

where $B(\overrightarrow{\mathbf{r}})$ is the magnetic flux value at point $\overrightarrow{\mathbf{r}}$ located on a defined surface. The ΔB values, obtained using (4.13), are reported in table (4.2).

FOV	ΔB(ppm)[a]	ΔB_{XY}(ppm)	ΔB_{XZ}(ppm)	ΔB_{YZ}(ppm)
Ellipsoid 40-60-40	2245	825	2245	2245
Ellipsoid 30-50-30	395	235	395	395
DSV40[b]	2245	250	2245	2245
DSV30	395	25	395	395
DSV20	40	15	40	40

Table 4.2: ΔB for the best solution of 0.2 T model

[a] Part Per Million
[b] Diameter of Spherical Volume

The results for the XY planes reported in table (4.2), which is the target plane for the optimization, are better improved compared to the other planes. The presence of a bored magnet pole causes a cold spot in the Z direction that can be addressed by further shimming.

Most of the patient's anatomy will fit in an ellipsoid with a major axis of 50 cm and a minor axes of 30 cm. The ΔB value for this surface is about 395 ppm. Magnetic field maps for this ellipsoid at different planes are shown in figure (4.8).

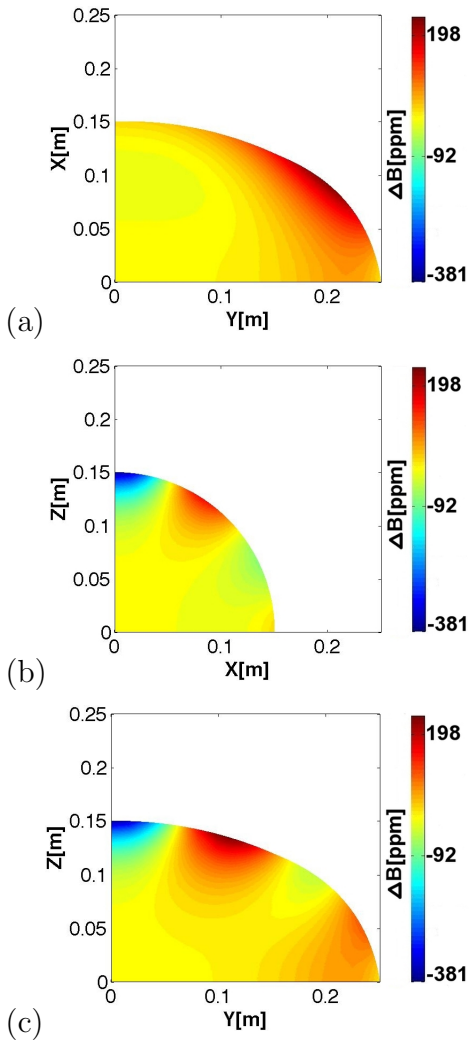

Figure 4.8: (a) Magnetic field map for the 0.2 T model for the XY plane of the ellipsoid 30-50-30 cm, (b) magnetic field map for the 0.2 T model for the ZX plane of the ellipsoid 30-50-30 cm, (c) magnetic field map for the 0.2 T model for the ZY plane of the ellipsoid 30-50-30 cm.

4.3.2 0.5 T Model Results

For the 0.5 T model, the optimization was started using the model with the pole plate as a bored cylinder. In this initial state, the Z value equal to 0.45 m was assigned to all control points on the pole plate. Figure (4.9a) shows the magnetic field map for a circle with diameter of 0.40 m in the XY plane when there is no bulk metal shim in the design. Figure (4.9b) shows the magnetic field map for a circle with diameter of 0.40 m in the XY plane after adding the bulk metal shim to let some of the flux pass through them. The magnetic force exerted on the bulk metal shim is calculated to be about 19 kN.

The objective function value defined by (4.9) is 2.25×10^{-2} for the bored cylinder as the pole plate. To speed-up the optimization process, the final solution for the 0.2 T magnet was considered as the initial solution for the final design. The objective function value for this solution is 2.84×10^{-4}, which is f_{val_i} for the first term of the optimization. After finishing optimization for all three terms of (4.12) using the PSO, a manual solution was added by the operator to prompt the simplex method to escape the local minimum in which the PSO seemed to get trapped. Based on the study of the XY plane map of the magnetic field for a circle with diameter of 60 cm, the thickness of the pole plate was manually adjusted at each control point to get a symmetrical map with a reasonable objective function. In addition to adjusting the thickness of the pole plate manually, the number of spokes were increased to nine to further smooth the pole plate in angular direction. As the points on one arc but different spokes are not independent, the number of parameters remained

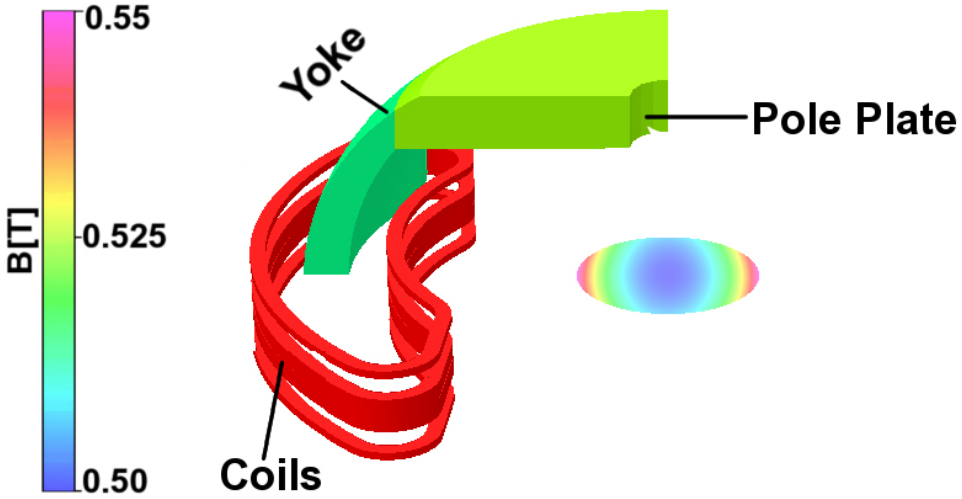

(a)

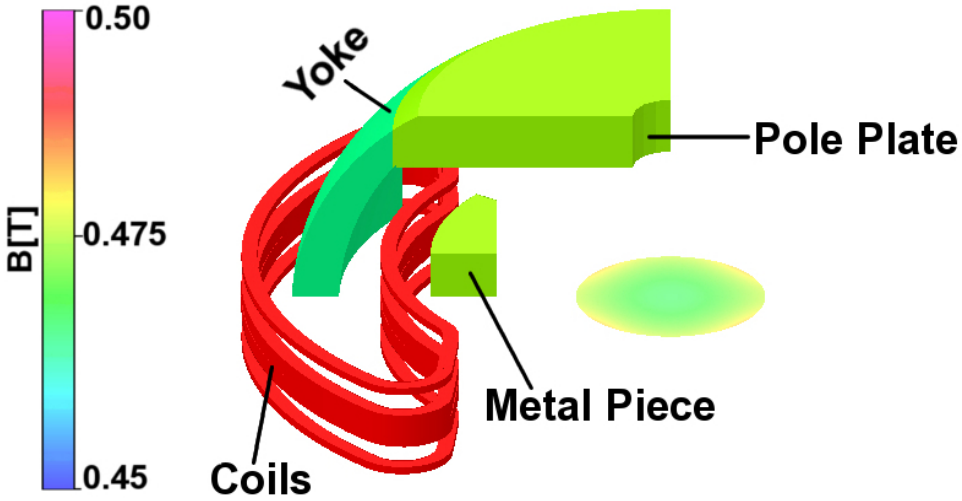

(b)

Figure 4.9: (a) Magnetic field map of the XY plane of an sphere with no bulk metal shims, (b) Magnetic field map of the XY plane of an sphere with added bulk metal shims.

the same when nine spokes were used.

The results for the minimization of the objective function are shown in table (4.3).

Pole Plate Structure	Cost Function using (4.9)		
Flat Pole Plate	$f = 2.25 \times 10^{-2}$		
	Optimization		
Projections	Algorithm	f_{val_i}	f_{val_f}
30 Projections - 5 Spokes	PSO-First Term	2.84×10^{-4}	2.16×10^{-4}
	PSO-Second Term	2.16×10^{-4}	1.69×10^{-4}
	PSO-Third Term	1.69×10^{-4}	8.59×10^{-5}
30 Projections - 9 Spokes	Manual Solution	1.37×10^{-4}	7.10×10^{-5}
	Simplex Method	7.10×10^{-5}	6.09×10^{-5}

Table 4.3: Optimization results

The inhomogeneities are calculated for the best solution of the 0.5 T model for different surfaces using (4.13) and the results are reported in table (4.4). The magnetic field maps for the ellipsoid 30-50-30 cm at different planes are shown in figure (4.10). The total ΔB value for this surface is 400 ppm.

FOV	ΔB(ppm)	ΔB_{XY}(ppm)	ΔB_{XZ}(ppm)	ΔB_{YZ}(ppm)
Ellipsoid 40-60-40	1370	1370	1150	980
Ellipsoid 30-50-30	400	320	300	140
DSV40	1150	240	1150	700
DSV30	300	65	300	90
DSV20	70	40	70	50

Table 4.4: ΔB for the best solution of the 0.5 T model using (4.13)

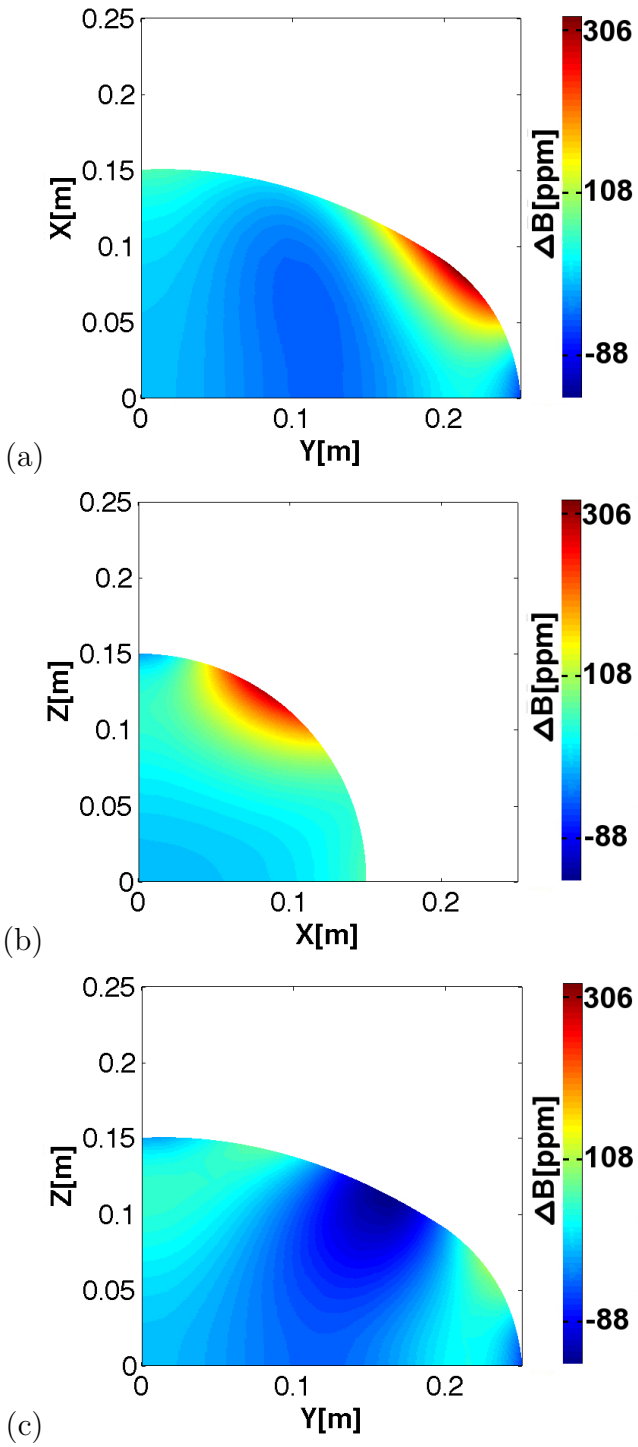

Figure 4.10: (a) Magnetic field map for the 0.5 T model for the XY plane of the ellipsoid 30-50-30 cm, (b) magnetic field map for the 0.5 T model for the ZX plane of the ellipsoid 30-50-30 cm, (c) magnetic field map for the 0.5 T model for the ZY plane of the ellipsoid 30-50-30 cm.

ΔB can be translated into spatial distortion using:

$$Spatial\ Distortion(SD) = \frac{\Delta B(mT)}{G(mT/m)}, \tag{4.14}$$

where G is the gradient strength measured in mT/m. The spatial distortions associated with the different gradient strengths, using ΔB values from table (4.4), are reported in table (4.5).

G(mT/m)	FOV	SD(mm)	SD_{XY}(mm)	SD_{XZ}(mm)	SD_{YZ}(mm)
10	Ellipsoid 40-60-40	69.5	65.9	58.3	49.7
	Ellipsoid 30-50-30	20.3	16.2	15.2	7.1
	DSV40	58.3	12.2	58.3	35.5
	DSV30	15.2	3.3	15.2	4.6
	DSV20	3.5	2.0	3.5	2.5
15	Ellipsoid 40-60-40	46.3	43.9	38.9	33.1
	Ellipsoid 30-50-30	13.5	10.8	10.1	4.7
	DSV40	38.9	8.1	38.9	23.7
	DSV30	10.1	2.2	10.1	3.0
	DSV20	2.4	1.4	2.4	1.7
20	Ellipsoid 40-60-40	34.7	33.0	29.2	24.8
	Ellipsoid 30-50-30	10.1	8.1	7.6	3.5
	DSV40	29.2	6.1	29.2	17.7
	DSV30	7.6	1.6	7.6	2.3
	DSV20	1.8	1.0	1.8	1.3

Table 4.5: Spatial distortions associated with different gradient strengths.

The spatial distortion is not sufficient for the final design implementation. However, it is standard MR practice to incorporate a system of passive and sometimes active shims to accommodate any remaining inhomogeneity for the magnetic field upon installation. These established techniques allow for reduction of the inhomogeneity significantly using passive shims. This involves the installation of magnetic pieces at the specific locations to correct for the

inhomogeneity. For example, in[70], the homogeneity is reduced by the order 10 using passive shimming and Jin et al.[71] showed the inhomogeneity reduction of the order 60 for DSV36 by applying passive shimming. Following this standard procedure, it is reasonable to expect improvement in the homogeneity. However, further work needs to be done.

While for diagnostic purposes, spatial distortions on the order of several millimeters will not affect the utility of the imaging, an accuracy of a millimetre or better is required for the radiotherapy[72;73]. When using the images from the larger field-of view, the residual distortion can be reduced to the sub-millimetre level by applying geometric correction algorithms to correct for the spatial distortion[72;73;74;75]. Using these algorithms to do further correction on the larger FOV regions, the magnet can also be used for the patient set-up.

Interaction of the field lines with the projections is illustrated in Figure (4.11) for the final solution of the pole plate.

It was showed that the presence of the field at the electron gun results in a target current loss in the parallel configuration[76]. In past designs, passive shielding has been implemented to reduce the field at the electron gun[77]. As can be seen in Figure (4.12), the field at the target is on the order of 400 G, meaning shielding at the linac would be essential for this model.

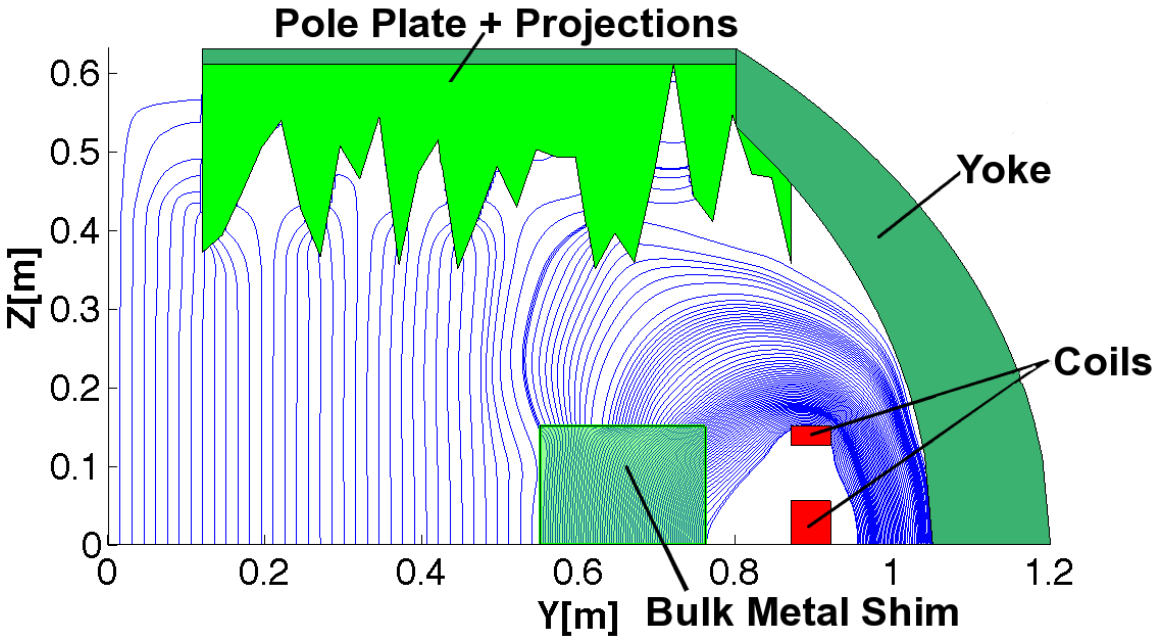

Figure 4.11: Interaction of the field lines with the projections for optimized pole plate.

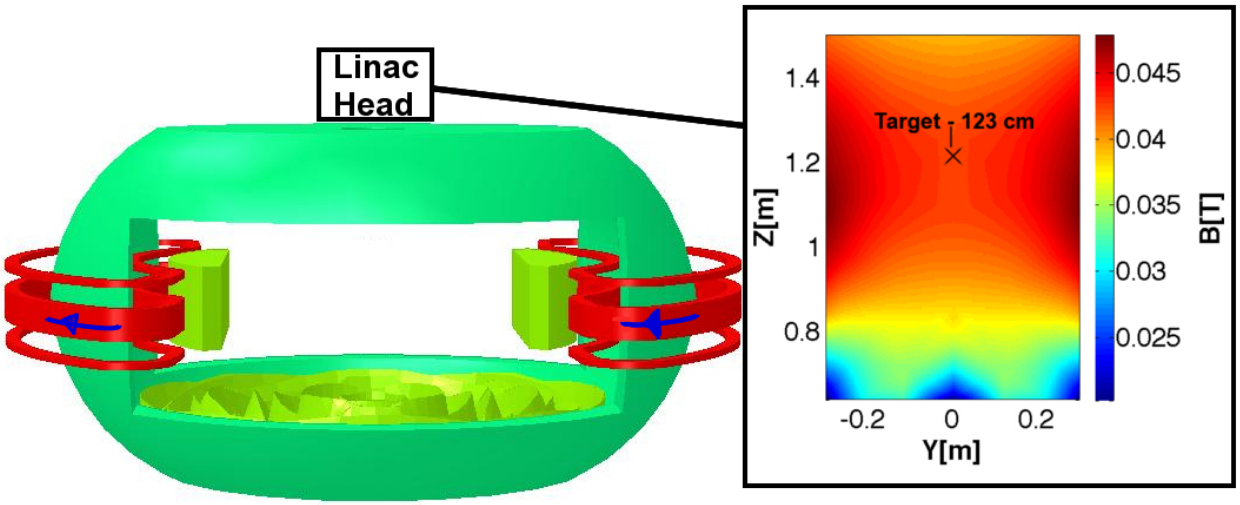

Figure 4.12: Field map at the Linac head for optimized pole plate.

Chapter 5

Conclusion and Future Directions

The Linac-MR system developed by Fallone et. al[17;18] is an advanced approach to real-time image guided radiation therapy. This unique rotating system with a bi-planar magnet can transmit radiation parallel to the magnetic field B_o. However, there are challenges to design a rotating bi-planar magnet as it should be compact with homogeneous field B_o and ample patient access. The work presented in this thesis proposed a novel design concept as a superconducting non-axial magnet, which could create a large uniform B_o field with fewer geometric restrictions.

Based on aforementioned design concept, the superconducting magnet was designed with a reduced SAD of 123 cm and a gap of 68 cm with the magnetic field of 0.5 T at isocentre. This novel design has several advantages over the current one[17]. The comparison between this new design and the current

system is summarized in table (5.1). The separation distance between two magnetic poles is larger so better accessibility and more room to accommodate the patient can be achieved. The magnet assembly is designed to be more compact in certain dimensions so the linac head can be moved closer to isocentre compared to the current magnet. This model is optimized to address the magnetic field homogeneity over a larger region; establishing the potential for a wider field-of-view. The final magnetic field is not sufficiently homogenous for raw implementation, but further passive shimming can be implemented to create a field capable of the use with radiotherapy.

Improvement	Current Design	New Design
SAD	130 cm	123 cm
Location of Coils	Pole Plate Area	Side of the Yoke
Opening Gap	60 cm	68 cm
FOV	DSV40	Ellipsoid 40-60-40
FOV - DSV40	6441 ppm	1150 ppm
Total Current	358 kA	3360 kA
Stored Energy	269 kJ	5622 kJ

Table 5.1: Comparison between the new design and the current system[17]

This non-axial design is in the early stages of development. Further optimization can maximize the benefit of this design. The yoke and pole plate structure can be further optimized to maximize the patient access, minimize the SAD, and reduce areas in the yoke saturated by the magnetic field. In addition, the current distribution needs to be further investigated and optimized to reduce the amount of superconducting material and the magnetic field inside the coil.

For the current model, the pole plate parameters are sampled uniformly in the radial direction. Exploring non-linear sampling such as logarithmic sampling for the pole plate in the radial direction to minimize sharp projections that may not have a large effect on homogeneity is the subject of the future work. In addition, modeling the variation of the control points in the radial direction, using different series such as sinusoidal or legendre polynomial series, can be explored as an alternative approach to reduce the number of parameters and minimize the sharpness of projections.

The complex structure of the pole plate surface would probably result in random errors during the manufacturing of the magnet. The stability of the final design can be investigated by adding random variations to the control points and yoke dimensions to test robustness of the field. In addition, the fluctuation of the magnetic field as a function of the temperature needs to be evaluated. To model the impact of temperature changes, the magnetic field calculation needs to done for the final design with different non-linear magnetization curves for different temperatures.

By moving the coils to the side, the cryostat is being moved away from the gradient coils. It is anticipated that the eddy currents might be reduced in the cryostat, which improves the efficiency of the gradient coils. This needs to be investigated for the final design.

Bibliography

[1] International Commission on Radiation Units and Measurements, "Prescribing, recording and reporting photon beam therapy," *Report 50*, ICRU, Bethesda,(1993).

[2] International Commission on Radiation Units and Measurements, "Prescribing, recording and reporting photon beam therapy," *Report 62*, ICRU, Bethesda,(1999).

[3] L. Dawson and D. Jaffray, "Advances in image-guided radiation therapy," *Journal of Clinical Oncology*, vol. 25, no. 8, pp. 938–946, (2007).

[4] D. Verellen, M. De Ridder, N. Linthout, K. Tournel, G. Soete, and G. Storme, "Innovations in image-guided radiotherapy," *Nature Reviews. Cancer*, vol. 7, no. 12, pp. 949–960, (2007).

[5] V. N. Hansen, P. M. Evans, and W. Swindell, "The application of transit dosimetry to precision radiotherapy," *Med. Phys.*, vol. 23, pp. 713–721, (1996).

[6] K. L. Pasma, B. J. Heijmen, M. Kroonwijk, and A. G. Visser, "Por-

tal dose image (PDI) prediction for dosimetric treatment verification in radiotherapy," *Med. Phys.*, vol. 25, pp. 830–840, (1998).

[7] H. Shirato, S. Shimizu, K. Kitamura, T. Nishioka, K. Kagei, S. Hashimoto, H. Aoyama, T. Kunieda, N. Shinohara, H. Dosaka-Akita, and K. Miyasaka, "Four-dimensional treatment planning and fluoroscopic real-time tumor tracking radiotherapy for moving tumor," *Int. J. Radiat. Oncol. Biol. Phys.*, vol. 48, pp. 435–442, (2000).

[8] T. R. Mackie, J. Kapatoes, K. Ruchala, W. G. Lu, C. Wu, G. Olivera, L. Forrest, W. Tome, J. Welsh, R. Jeraj, P. Harari, P. Reckwerdt, B. Paliwal, M. Ritter, H. Kellar, J. Fowler, and M. Metha, "Image guidance for precise conformal radiotherapy," *Int. J. Radiat. Oncol. Biol. Phys.*, vol. 56, pp. 89–105, (2003).

[9] K. M. Langen, S. L. Meeks, D. O. Poole, T. H. Wagner, T. R. Willoughby, P. A. Kupelian, K. J. Ruchala, J. Haimerl, and G. H. Olivera, "The use of megavoltage CT (MVCT) images for dose recomputations," *Phys. Med. Biol.*, vol. 50, pp. 4259–4276, (2005).

[10] E. J. Holupka, I. D. Kaplan, E. C. Burdette, and G. K. Svensson, "Ultrasound image fusion for external beam radiotherapy for prostate cancer," *Int. J. Radiat. Oncol. Biol. Phys.*, vol. 35, pp. 975–984, (1996).

[11] J. Lattanzi, S. McNeeley, W. Pinover, E. Horwitz, I. Das, T. E. Schultheiss, and G. E. Hanks, "A comparison of daily CT localization to a daily ultrasound-based system in prostate cancer," *Int. J. Radiat. Oncol. Biol. Phys.*, vol. 43, pp. 719–725, (1999).

[12] F. Khan, *The Physics of Radiation Therapy.* Lippincott Williams & Wilkins, 5th ed., (2010).

[13] P. G. Seiler, H. Blattmann, S. Kirsch, R. K. Muench, and S. C., "A novel tracking technique for the continuous precise measurement of tumour positions in conformal radiotherapy," *Phys. Med. Biol.*, vol. 45, pp. N103–N110, (2000).

[14] J. F. Dempsey, D. Benoit, J. Fitzsimmons, A. Haghighat, J. G. Li, D. A. Low, S. Mutic, J. R. Palta, H. Romeijn, and G. Sjoden, "A device for realtime 3D image-guided IMRT," *Int. J. Radiat. Oncol. Biol. Phys.*, vol. 63, no. 2, p. S202, (2005).

[15] P. J. Keall, M. Barton, and S. Crozier, "The australian magnetic resonance imaging-linac program," *Semin. Radiat. Oncol.*, vol. 24, pp. 203–206, (2014).

[16] B. W. Raaymakers, J. J. W. Lagendijk, J. Overweg, J. G. M. Kok, A. J. E. Raaijmakers, E. M. Kerkhof, R. W. van der Put, I. Meijsing, S. P. M. Crijns, B. F., M. van Vulpen, C. H. W. de Graaff, J. Allen, and K. J. Brown, "Integrating a 1.5 T MRI scanner with a 6 MV accelerator: proof of concept," *Phys. Med. Biol.*, vol. 54, no. 12, p. N229, (2009).

[17] B. G. Fallone, "The rotating biplanar linac-magnetic resonance imaging system," *Semin Radiat Oncol*, vol. 24, pp. 200–202, (2014).

[18] A. Keyvanloo, B. Burke, J. St. Aubin, D. Baillie, K. Wachowicz, B. Warkentin, S. Steciw, and B. G. Fallone, "Minimal skin dose increase

in longitudinal rotating biplanar linac-MR systems: examination of radiation energy and flattening filter design," *Phys. Med. Biol.*, vol. 61, no. 9, pp. 3527–3539, (2016).

[19] S. Mutic and J. F. Dempsey, "The ViewRay system: Magnetic resonance-guided and controlled radiotherapy," *Semin. Radiat. Oncol.*, vol. 24, no. 3, pp. 196–199, (2014).

[20] O. Pechenaya Green, S. Goddu, and S. Mutic, "Commissioning and quality assurance of the first commercial hybrid MRI-IMRT system," *Med. Phys.*, vol. 39, no. 6, p. 3785, (2012).

[21] J. J. W. Lagendijk, M. van Vulpen, and B. W. Raaymakers, "The development of the MRI linac system for online MRI-guided radiotherapy: a clinical update," *J Intern Med.*, vol. 280, no. 2, pp. 203–208, (2016).

[22] A. J. E. Raaijmakers, B. W. Raaymakers, and J. J. W. Lagendijk, "Integrating a MRI scanner with a 6 MV radiotherapy accelerator: dose increase at tissue-air interfaces in a lateral magnetic field due to returning electrons," *Phys. Med. Biol.*, vol. 50, pp. 1363–76, (2005).

[23] C. Kirkby, T. Stanescu, S. Rathee, M. Carlone, B. Murray, and B. G. Fallone, "Patient dosimetry for hybrid MRI-radiotherapy systems," *Med. Phys.*, vol. 35, pp. 1019–1027, (2008).

[24] B. G. Fallone, B. Murray, S. Rathee, T. Stanescu, S. Steciw, S. Vidakovic, E. Blosser, and D. Tymofichuk, "First MR images obtained during megavoltage photon irradiation from a prototype integrated linac-MR system," *Med. Phys.*, vol. 36, no. 6, pp. 2084–2088, (2009).

[25] D. W. Litzenberg, B. A. Fraass, D. L. McShan, T. W. O'Donnell, D. A. Roberts, F. D. Becchetti, A. F. Bielajew, and J. M. Moran, "An apparatus for applying strong longitudinal magnetic fields to clinical photon and electron beams," *Phys. Med. Biol.*, vol. 46, pp. N105–N1158, (2001).

[26] C. Kirkby, B. Murray, S. Rathee, and B. G. Fallone, "Lung dosimetry in a linac-MRI radiotherapy unit with a longitudinal magnetic field," *Med. Phys.*, vol. 37, pp. 4722–4732, (2010).

[27] T. Tadic and B. G. Fallone, "Design and optimization of a novel bored biplanar permanent magnet assembly for hybrid MRI systems," *IEEE Trans. Magn.*, vol. 46, no. 12, pp. 4052–4058, (2010).

[28] T. Tadic and B. G. Fallone, "Three-dimensional nonaxisymmetric pole piece shape optimization for biplanar permanent magnet MRI systems," *IEEE Trans. Magn.*, vol. 47, no. 1, pp. 231–238, (2011).

[29] K. Wachowicz, B. Murray, and B. G. Fallone, "Peripheral tumour treatment," *US Patent 2016/0228727A1*, (2016).

[30] Opera-3D, *version 13.0*. Vector Fields, Oxford, (2007).

[31] V. Kuperman, *Magnetic Resonance Imaging: Physical Principles and Applications*. Academic Press Series in Electromagnetism, Academic Press, (2000).

[32] R. W. Brown, Y. N. Cheng, E. M. Haacke, M. R. Thompson, and R. Venkatesan, *Magnetic Resonance Imaging: Physical Principles and Sequence Design*. John Wiley & Sons Inc., 2nd ed., (2014).

[33] E. Berry and A. Bulpitt, *Fundamentals of MRI: An Interactive Learning Approach*. Series in Medical Physics and Biomedical Engineering, Taylor & Francis, (2008).

[34] D. Dowsett, P. Kenny, and R. Johnston, *The Physics of Diagnostic Imaging Second Edition*. A Hodder Arnold Publication, Taylor & Francis, (2006).

[35] C. Collins, *Electromagnetics in Magnetic Resonance Imaging: Physical Principles, Related Applications, and Ongoing Developments*. Morgan & Claypool Publishers, (2016).

[36] F. Romeo and D. I. Hoult, "Magnet field profiling: Analysis and correcting coil design," *Magn. Reson. Med.*, vol. 1, no. 1, pp. 44–65, (1984).

[37] K. Wachowicz, T. Tadic, and B. G. Fallone, "Geometric distortion and shimming considerations in a rotating MR-linac design due to the influence of low-level external magnetic fields," *Med. Phys.*, vol. 39, no. 5, pp. 2659–2668, (2012).

[38] P. Jezzard, "Shim coil design, limitations and implications," *Abstracts from the International Society of Magnetic Resonance in Medicine (ISMRM) Annual Meeting*, (2006).

[39] J. Nagamatsu, N. Nakagawa, T. Muranaka, Y. Zenitani, and A. J., "Superconductivity at 39 K in magnesium diboride," *Nature*, vol. 410, pp. 63–64, (2001).

[40] M. Razeti, S. Angius, L. Bertora, D. Damiani, R. Marabotto, M. Modica, D. Nardelli, M. Perrella, and M. Tassisto, "Construction and operation of

cryogen free MgB_2 magnets for open MRI systems," *IEEE Trans. Appl. Supercond.*, vol. 18, no. 2, (2008).

[41] J. Jin, *The Finite Element Method in Electromagnetics*. New York: John Wiley & Sons Inc., 2nd ed., (2002).

[42] O. C. Zienkiewicz, R. L. Taylor, and Z. Zhu, *The Finite Element Method: Its Basis and Fundamentals*. Oxford: Elsevier, 6th ed., (2005).

[43] S. C. Brenner and L. R. Scott, *The Mathematical Theory of Finite Element Methods*. New York: Springer, 3rd ed., (2008).

[44] E. Onate, J. Periaux, and A. Samuelsson, *The finite element method in the 1990'S (A Book Dedicated to O.C. Zienkiewicz)*. Barcelona: CIMNE, 1st ed., (1991).

[45] J. D. Jackson, *Classical electrodynamics*. New York, NY: Wiley, 3rd ed., (1999).

[46] J. Simkin and C. W. Trowbridge, "On the use of the total scalar potential in the numerical solution of field problems in electromagnetics," *International Journal for Numerical Methods in Engineering*, vol. 14, pp. 423–440, (1979).

[47] J. Simkin and C. W. Trowbridge, "Three-dimensional nonlinear electromagnetic field computations, using scalar potentials," *IEE PROC*, vol. 127 pt. B, no. 6, pp. 368–374, (1980).

[48] A. Antoniou and W. Lu, *Practical Optimization: Algorithms and Engineering Applications*. Springer US, (2010).

[49] S. M. Mikki and A. A. Kishk, *Particle Swarm Optimization: A Physics-based Approach*. Morgan & Claypool, (2008).

[50] M. P. Friedlander and M. Schmidt, "Hybrid deterministic-stochastic methods for data fitting," *SIAM Journal on Scientific Computing (SISC)*, (2012).

[51] J. Kennedy and R. C. Eberhart, "Particle swarm optimization," in *Proceedings of the IEEE International Conference on Neural Networks*, pp. 1942–1948, (1995).

[52] S. Kiranyaz, T. Ince, and M. Gabbouj, *Multidimensional Particle Swarm Optimization for Machine Learning and Pattern Recognition*. Springer Berlin Heidelberg, (2013).

[53] Y. Shi and R. C. Eberhart, "A modified particle swarm optimizer," *Proc. IEEE World Congr. Comput. Intell.*, pp. 69–73, (1998).

[54] M. Clerc and K. J., "The particle swarm-explosion, stability and convergence in a multidimensional complex space," *IEEE Trans. Evol. Comput.*, vol. 6, no. 1, pp. 58–73, (2002).

[55] I. C. Trelea, "The particle swarm optimization algorithm: Convergence analysis and parameter selection," *Inf. Process. Lett.*, vol. 85, no. 6, pp. 317–325, (2003).

[56] J. Kennedy, R. C. Eberhart, and Y. H. Shi, *Swarm Intelligence*. San Mateo, CA: Morgan Kaufmann, (2001).

[57] Z. H. Zhan, J. Zhang, Y. Li, and C. H. S., "Adaptive particle swarm optimization," *IEEE Trans. Syst., Man, Cybern. B*, vol. 39, no. 6, pp. 1362–1381, (2009).

[58] C. F. Juang, "A hybrid of genetic algorithm and particle swarm optimization for recurrent network design," *IEEE Trans. Syst. Man. Cybern B: Cybern*, vol. 34, no. 2, pp. 997–1006, (2004).

[59] J. J. Liang, A. K. Qin, P. N. Suganthan, and S. Baskar, "Comprehensive learning particle swarm optimizer for global optimization of multimodal functions," *IEEE Trans. Evol. Comput.*, vol. 10, no. 3, pp. 281–295, (2006).

[60] V. Torczon, "On the convergence of pattern search algorithms," *SIAM J. OPTIM.*, vol. 7, no. 1, pp. 1–25, (1997).

[61] J. A. Nelder and R. Mead, "A simplex method for function minimization," *Computer Journal*, vol. 7, pp. 303–318, (1965).

[62] J. H. Mathews and K. K. Fink, *Numerical Methods Using Matlab*. New Jersey, USA: Prentice-Hall Inc., (2004).

[63] J. Lagarias, J. A. Reeds, M. H. Wright, and P. E. Wright, "Convergence properties of the Nelder-Mead simplex method in low dimensions," *SIAM Journal of Optimization*, vol. 9, no. 1, pp. 112–147, (1998).

[64] MATLAB, *version 7.12.0 (R2011a)*. Natick, Massachusetts: The MathWorks Inc., (2011).

[65] D. Dorner, S. Zaefferer, L. Lahn, and D. Raabe, "Overview of microstructure and microtexture development in grain-oriented silicon steel," *Journal of Magnetism and Magnetic Materials*, vol. 304, no. 2, pp. 183 – 186, (2006).

[66] T. Tadic and B. G. Fallone, "Design and optimization of superconducting MRI magnet systems with magnetic materials," *IEEE Appl. Supercond.*, vol. 22, no. 2, p. 4400107, (2012).

[67] G. Z. Li, M. Susner, S. D. Bohnenstiehl, M. Sumption, and E. Collings, "Microstructures and superconducting properties of high performance MgB_2 thin films deposited from a high-purity, dense Mg-B target," *Applied Surface Science*, vol. 357, pp. 452–458, (2015).

[68] J. R. Brauer, *Magnetic Actuators and Sensors, Appendix B: nonlinear B–H curves*. Hoboken, NJ: Wiley, 2nd ed., (2013).

[69] N. B. S. Gloria, M. C. L. Areiza, I. V. J. Miranda, and J. M. A. Rebello, "Development of a magnetic sensor for detection and sizing of internal pipeline corrosion defects," *NDTE Int.*, vol. 42, pp. 669–77, (2009).

[70] X. C. Zhu, H. S. Wang, H. Wang, and Y. Li, "A novel passive shimming method for 0.7 T biplanar superconducting MRI," *Proceedings of IEEE International Conference on ASMED*, pp. 418–419, (2015).

[71] Z. Jin, X. Tang, B. Meng, D. Zu, and W. Wang, "A SQP optimization method for shimming a permanent MRI magnet," *Progress in Natural Science*, vol. 19, pp. 1439–1443, (2009).

[72] M. Breeuwer, M. Holden, and W. Zylka, "Detection and correction of geometric distortion in 3D MR images," *Proc. SPIE*, vol. 4322, pp. 1110–1120, (2001).

[73] L. N. Baldwin, K. Wachowicz, S. D. Thomas, R. Rivest, and B. G. Fallone, "Characterization, prediction, and correction of geometric distortion in 3 T MR images," *Med. Phys.*, vol. 34, no. 2, pp. 3917–3926, (2007).

[74] S. J. Doran, E. M. Charles-Edwards, S. A. Reinsberg, and M. O. Leach, "A complete distortion correction for MR images. I. gradient warp correction," *Phys. Med. Biol.*, vol. 50, pp. 1343–1361, (2005).

[75] D. Wang, D. M. Doddrell, and G. Cowin, "A novel phantom and method for comprehensive 3-dimensional measurement and correction of geometric distortion in magnetic resonance imaging," *Magn. Reson. Imaging*, vol. 22, pp. 529–542, (2004).

[76] J. St. Aubin, D. M. Santos, S. Steciw, and B. G. Fallone, "Effect of longitudinal magnetic fields on a simulated in-line 6 mv linac," *Med. Phys.*, vol. 37, pp. 4916–4923, (2010).

[77] D. M. Santos, J. St. Aubin, S. Steciw, and B. G. Fallone, "Magnetic shielding investigation for a 6 mv in-line linac within the parallel configuration of a linac-mr system," *Med. Phys.*, vol. 39, pp. 788–97, (2012).

Appendix A

Finite Element Formulation for a 2D Element

An example is presented to show how the elemental function for a linear triangular element (as shown in figure (A.1)) is determined[41]. The polynomial Lagrange function, $u^e(x, y)$, for this element is defined as:

$$u^e(x, y) = a_1^e + a_2^e\ x + a_3^e\ y, \tag{A.1}$$

where a_1^e, a_2^e, and a_3^e are unknown constant coefficients. To determine the unknown coefficients, the values of $u^e(x, y)$ at three nodal points are used to form a system of equations as follows:

$$u^e(x_1^e, y_1^e) = a_1^e + a_2^e\ x_1^e + a_3^e\ y_1^e, \tag{A.2a}$$

$$u^e(x_2^e, y_2^e) = a_1^e + a_2^e\ x_2^e + a_3^e\ y_2^e, \tag{A.2b}$$

$$u^e(x_3^e, y_3^e) = a_1^e + a_2^e\ x_3^e + a_3^e\ y_3^e, \tag{A.2c}$$

where (x_i^e, y_i^e) is the coordinate value for the nodal point i $(i = 1, 2, 3)$, shown in figure (A.1). The nodal points are numbered in a counterclockwise manner.

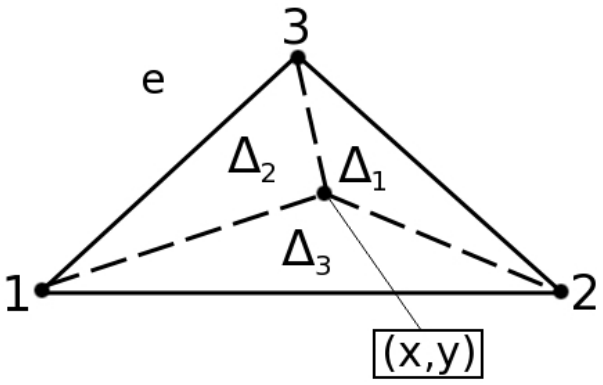

Figure A.1: Example of a triangular element e

Using equations (A.2a) - (A.2c), the unknown coefficients of equation (A.1) are found in terms $u^e(x_i^e, y_i^e)$. Substituting these coefficients back into equation (A.1), the $u^e(x, y)$ is expressed as:

$$u^e(x, y) = \sum_{i=1}^{3} u_i^e \ \lambda_i^e(x, y), \tag{A.3}$$

where u_i^e is $u^e(x_i^e, y_i^e)$, and $\lambda_i^e(x, y)$ is defined as :

$$\lambda_i^e(x, y) = \frac{\Delta_i}{\Delta^e}, \tag{A.4}$$

where Δ_i is the area of sub-triangle i within element e and Δ^e is the area of the triangular element e. Sub-triangle i is formed when the point (x, y) is replaced by nodal point i.

The location of point (x, y) inside the element e is given by equation (A.4) in the barycentric coordinate system as: $(\frac{\Delta_1}{\Delta^e}, \frac{\Delta_2}{\Delta^e}, \frac{\Delta_2}{\Delta^e})$. As mentioned before, the $\lambda_i^e(x_j, y_j) = \delta_{ij}$ for nodal point (x_j, y_j). In addition, it can be shown that $\lambda_i^e(x, y) = 0$ if point (x, y) is located on the element side opposite to node i.

Using the coordinate values of nodal points and (A.4), $\lambda_i^e(x, y)$ is calculated as:

$$\lambda_i^e(x, y) = \frac{1}{2\Delta^e}(a_{1i}^e + a_{2i}^e\ x + a_{3i}^e\ y), \tag{A.5}$$

where:

$$a_{11}^e = x_2^e\ y_3^e - x_3^e\ y_2^e; \qquad a_{21}^e = y_2^e - y_3^e; \qquad a_{31}^e = x_3^e - x_2^e, \tag{A.6a}$$

$$a_{12}^e = x_3^e\ y_1^e - x_1^e\ y_3^e; \qquad a_{22}^e = y_3^e - y_1^e; \qquad a_{32}^e = x_1^e - x_3^e, \tag{A.6b}$$

$$a_{13}^e = x_1^e\ y_2^e - x_2^e\ y_1^e; \qquad a_{23}^e = y_1^e - y_2^e; \qquad a_{33}^e = x_2^e - x_1^e. \tag{A.6c}$$

The area of a triangle is calculated using the following determinant:

$$\Delta^e = \frac{1}{2}\begin{vmatrix} 1 & x_1^e & y_1^e \\ 1 & x_2^e & y_2^e \\ 1 & x_3^e & y_3^e \end{vmatrix}. \tag{A.7}$$

Having the elemental basis function determined, the contribution of this element to the stiffness matrix K and the load matrix F are evaluated using

(2.26) as follows:

$$K_{ij}^e = \int_{\Omega^e} \bigtriangledown \lambda_i^e \cdot \alpha \bigtriangledown \lambda_j^e \, d\Omega^e, \tag{A.8a}$$

$$F_i^e = \int_{\Omega^e} f \lambda_j^e \, d\Omega^e. \tag{A.8b}$$

Using equation (A.5), the K_{ij}^e and F_i^e are:

$$K_{ij}^e = \frac{\alpha}{4\Delta^e}(a_{2i}^e a_{2j}^e + a_{3i}^e a_{3j}^e), \tag{A.9a}$$

$$F_i^e = \frac{\Delta^e}{3} f, \tag{A.9b}$$

where α and f are assumed to be constants within the element $e^{(41)}$.